

**IOT-INSPIRED SPECTRUM SHARING IN  
UAV-ASSISTED NOMA NETWORKS WITH  
DEEP LEARNING APPROACH**

**MS (Research) Thesis**

*by*

**RATNESH KUMAR**



**DEPARTMENT OF ELECTRICAL ENGINEERING  
INDIAN INSTITUTE OF TECHNOLOGY INDORE**

**MAY 2023**



**IOT-INSPIRED SPECTRUM SHARING IN  
UAV-ASSISTED NOMA NETWORKS WITH  
DEEP LEARNING APPROACH**

**A THESIS**

*Submitted in fulfillment of the  
requirements for the award of the degree*

*of*

**Master of Science (Research)**

*by*

**RATNESH KUMAR**



**DEPARTMENT OF ELECTRICAL ENGINEERING  
INDIAN INSTITUTE OF TECHNOLOGY INDORE  
MAY 2023**





# INDIAN INSTITUTE OF TECHNOLOGY INDORE

## CANDIDATE'S DECLARATION

I hereby certify that the work which is being presented in the thesis entitled “**IOT-INSPIRED SPECTRUM SHARING IN UAV-ASSISTED NOMA NETWORKS WITH DEEP LEARNING APPROACH**” in the fulfillment of the requirements for the award of the degree of **MASTER OF SCIENCE (RESEARCH)** and submitted in the **DEPARTMENT OF ELECTRICAL ENGINEERING, Indian Institute of Technology Indore**, is an authentic record of my own work carried out during the time period from August 2021 to Jun 2023 under the supervision of Prof. Prabhat Kumar Upadhyay, Professor, Department of Electrical Engineering, Indian Institute of Technology Indore, India.

The matter presented in this thesis has not been submitted by me for the award of any other degree of this or any other institute.

Ratnesh Kumar  
27-05-2023

Signature of the student with date  
(**RATNESH KUMAR** )

-----  
This is to certify that the above statement made by the candidate is correct to the best of my/our knowledge.

  
27-05-2023

Signature of Thesis Supervisor with date  
(**Prof. PRABHAT KUMAR UPADHYAY**)

-----  
Signature of Chairperson (OEB)



Signature of Thesis Supervisor

Signature of Convener, DPGC

Signature of Head of Discipline



## ACKNOWLEDGEMENTS

I would like to thank everyone from the bottom of my heart. Who had supported me, both directly and indirectly, during my MS (Research) program. To begin with, I express my gratitude to God Almighty for providing me with the ability, understanding, and illumination to carry out this research. Additionally, I want to convey my profound admiration and appreciation to my thesis advisor and mentor, Prof. Prabhat Kumar Upadhyay, for his priceless direction, unwavering encouragement, and benevolent assistance in my academic pursuits. Throughout my tenure at IIT Indore, he has granted me complete independence to pursue my research and offered valuable career guidance and suggestions that transcend academic boundaries whenever I sought it. I have always found him to be a great inspiration, and will continue to be for the rest of my life.

During my research, Dr. Trapti Jain, a professor in the Department of Electrical Engineering, and Dr. Santosh Kumar Sahu, a professor in the Department of Mechanical Engineering, both from IIT Indore, offered valuable input on the evaluation of my work, and I am grateful to them. Throughout my thesis work, I received great cooperation from all the faculty members and staff at IIT Indore, for which I am truly grateful.

I would like to express my gratitude to the Wireless Communications (WiCom) research group members for creating a welcoming and favorable atmosphere. I had the honor of working alongside Chandan Kumar Singh, Alok Kumar Shukla, Kajal Yadav, and Cheepurupalli Shivaji in the lab, and it was a great privilege. Additionally, I express my gratitude towards my colleagues Akash, Prashant, and Vivek, who have been amazing friends and shared the special moments of my life at IIT Indore. My gratitude goes to the Ministry of Human Resource Development (MHRD), Government of India and IIT Indore for extending financial assistance. Additionally, I would like to express my appreciation to the finance, administration, academic, and R&D departments for their valuable support. Finally, my heartfelt thanks go out to all who have assisted me along the way, those who contributed to this journey and supported me in various ways, enabling me to accomplish this research work successfully.

RATNESH KUMAR

*Dedicated to  
my family*



# ABSTRACT

Energy and spectral efficiency (SE) of Internet of Things (IoT) networks can be improved by integrating energy harvesting, cognitive radio, and non-orthogonal multiple access (NOMA) techniques, while unmanned aerial vehicles (UAVs), on the other hand, are a quick and adaptable entity for improving the coverage performance. We conducted a study to assess the performance of an overlay cognitive radio-NOMA (OC-NOMA) system assisted by UAVs using an energy harvesting-based cooperative spectrum sharing transmission (I-CSST) scheme, inspired by the IoT. Herein, an energy-constrained UAV-borne secondary node harvests radio-frequency energy from the primary source (PS) and uses it to send both its own information signal and the primary information signal using the NOMA approach. We consider the impact of the imperfect successive interference cancellation (iSIC) in NOMA and the distortion noises caused by hardware impairments (HIs) in signal processing, which are unavoidable in real-world systems. We obtain the complicated expressions of outage probability (OP) for primary and secondary IoT networks using I-CSST scheme under heterogeneous Rician and Nakagami- $m$  fading channels. We continue to investigate asymptotic analysis for OP in order to gain insightful knowledge on the high signal-to-noise ratio (SNR) slope and practicable diversity order. We also assess the system throughput and energy efficiency for the considered OC-NOMA system. Our results demonstrate the benefits of the suggested I-CSST scheme over the benchmark primary direct transmission (PDT) and orthogonal multiple access schemes (OMA). We create a deep neural network (DNN) architecture for real-time OP prediction in order to combat the complications in model-based approaches.

Above all, this thesis focuses on the technical aspects involved in the implementation of the OC-NOMA system and provides valuable insights for practical system design. The proposed schemes, strategies, and theoretical developments aim to enhance the SE and reliability of the OC-NOMA system, making it suitable for future wireless network applications.

<b>LIST OF FIGURES</b>	<b>v</b>
<b>LIST OF SYMBOLS</b>	<b>vi</b>
<b>LIST OF ABBREVIATIONS</b>	<b>viii</b>
<b>1 Introduction</b>	<b>1</b>
1.1 Cognitive Radio . . . . .	2
1.2 Cooperative Relaying . . . . .	3
1.2.1 Fixed Relaying . . . . .	3
1.3 Non-Orthogonal Multiple Access . . . . .	3
1.4 Unmanned Aerial Vehicles . . . . .	4
1.5 System Imperfections . . . . .	4
1.6 Background Works . . . . .	5
1.7 Motivation and Objectives . . . . .	7
1.7.1 Motivation . . . . .	7
1.7.2 Objectives . . . . .	8
1.8 Contributions . . . . .	9
1.9 Organization of the Thesis . . . . .	10
<b>2 System Descriptions and Performance Analysis</b>	<b>12</b>
2.1 System Model and I-CSST Scheme Description . . . . .	13
2.1.1 System and Channel Models . . . . .	13
2.1.2 PS-Based EH with Source Transmission . . . . .	16
2.1.3 DF Relaying with OC-NOMA Transmission . . . . .	18
2.2 Performance Analysis of Primary Network . . . . .	20
2.2.1 Accurate OP Analysis . . . . .	20
2.2.2 Asymptotic OP Analysis . . . . .	23
2.2.3 NOMA Power Allocation Parameter . . . . .	24
2.3 Performance Analysis of Secondary Network . . . . .	24
2.3.1 Accurate OP Analysis . . . . .	25
2.3.2 Asymptotic OP Analysis . . . . .	27
2.4 Overall OC-NOMA System Performance . . . . .	28
2.4.1 System Throughput . . . . .	28
2.4.2 Energy Efficiency . . . . .	29

<b>3</b>	<b>Deep Learning Analysis</b>	<b>31</b>
3.1	Deep Neural Network Design . . . . .	31
3.1.1	Dataset Generation Technique . . . . .	32
3.1.2	DNN Architecture . . . . .	33
3.1.3	Real-Time Prediction of OP . . . . .	34
<b>4</b>	<b>Numerical and Simulation Investigation</b>	<b>36</b>
4.1	Numerical and Simulation Results . . . . .	36
4.2	Summary . . . . .	41
<b>5</b>	<b>Conclusions and Future Scope</b>	<b>44</b>
5.1	Conclusions . . . . .	44
5.2	Future Scope . . . . .	45
	<b>Appendix A Derivation of (2.28)</b>	<b>48</b>
	<b>Appendix B Derivation of (2.41)</b>	<b>49</b>
	<b>REFERENCES</b>	<b>51</b>
	<b>LIST OF PUBLICATIONS</b>	<b>58</b>



## LIST OF FIGURES

2.1	OC-NOMA system model. . . . .	13
2.2	Transmission block structure for the PS-based EH. . . . .	16
3.1	DNN deployment architecture. . . . .	32
4.1	OP performance of the primary network. . . . .	38
4.2	OP performance of the secondary network. . . . .	39
4.3	OP performance comparison of NOMA with OMA. . . . .	40
4.4	Throughput plots for OC-NOMA system. . . . .	41
4.5	Energy efficiency plots for OC-NOMA system. . . . .	42

# List of Symbols

- Basic arithmetic and calculus notations have standard definitions.

## Elementary & Special Functions

---

---

Notation	Definition
$\Gamma(\cdot)$	Gamma function
$\Upsilon(\cdot, \cdot)$	Lower incomplete Gamma function
$\Gamma(\cdot, \cdot)$	Upper incomplete Gamma function
$\mathcal{K}_\nu(\cdot)$	Modified Bessel function of the second kind of order $\nu$
$\log_i(\cdot)$	Logarithm to base $i$

---

## Probability & Statistics

Let  $X$  be a random variable, and  $\mathcal{A}$  be an arbitrary event.

---

---

Notation	Definition
$\mathbb{E}(\cdot)$	Expectation
$f_X(\cdot)$	Probability density function (PDF) of $X$
$F_X(\cdot)$	Cumulative distribution function (CDF) of $X$
$\Pr[\mathcal{A}]$	Probability of $\mathcal{A}$
$X \sim \mathcal{CN}(\mu, \sigma^2)$	$X$ is complex Gaussian distributed with mean $\mu$ and variance $\sigma^2$

---

## Miscellaneous

---

---

Notation	Definition
$n!$	Factorial of $n$
$\mathcal{C}_r^n = \binom{n}{r} = \frac{n!}{r!(n-r)!}$	Binomial coefficient

---



# List of Abbreviations

<b>1G</b>	First-Generation
<b>2-D</b>	Two-Dimensional
<b>3-D</b>	Three-Dimensional
<b>5G</b>	Fifth-Generation
<b>6G</b>	Sixth-Generation
<b>AF</b>	Amplify-and-Forward
<b>AI</b>	Artificial Intelligence
<b>AWGN</b>	Additive White Gaussian Noise
<b>BS</b>	Base Station
<b>CDF</b>	Cumulative Distribution Function
<b>CEEs</b>	Channel Estimation Errors
<b>C-NOMA</b>	Cooperative NOMA
<b>CR</b>	Cognitive Radio
<b>CR-NOMA</b>	Cognitive NOMA
<b>CSI</b>	Channel Status Information
<b>DF</b>	Decode-and-Forward
<b>DNN</b>	Deep Neural Network
<b>DL</b>	Deep Learning
<b>DLS</b>	Damped Least-Squares
<b>EH</b>	Energy Harvesting
<b>eLU</b>	Exponential Linear Unit
<b>HD</b>	Half-Duplex
<b>HIs</b>	Hardware Impairments
<b>i.i.d.</b>	Independent and Identically Distributed
<b>I-CSST</b>	IoT-inspired cooperative spectrum sharing transmission
<b>IoT</b>	Internet of Things
<b>I/Q</b>	In-Quadrature-Phase
<b>IP</b>	Information Processing
<b>iSIC</b>	Imperfect SIC
<b>LI</b>	Residual Loop Self-Interference
<b>LoS</b>	Line-of-Sight
<b>ML</b>	Machine Learning
<b>MSE</b>	Mean Squared Error

<b>MRC</b>	Maximal Ratio Combining
<b>NOMA</b>	Non-Orthogonal Multiple Access
<b>O-CR</b>	Overlay Cognitive Radio
<b>OC-NOMA</b>	Overlay CR-NOMA
<b>OMA</b>	Orthogonal Multiple Access
<b>OP</b>	Outage Probability
<b>PDF</b>	Probability Density Function
<b>PDT</b>	Primary Direct Transmission
<b>PR</b>	Primary Receiver
<b>pSIC</b>	Perfect SIC
<b>PS</b>	Power-Splitting
<b>PT</b>	Primary Transmitter
<b>PU</b>	Primary User
<b>QoS</b>	Quality-of-Service
<b>RF</b>	Radio-Frequency
<b>RMSE</b>	root-mean-square error
<b>SE</b>	Spectral-Efficiency
<b>SIC</b>	Successive Interference Cancellation
<b>SINR</b>	Signal-to-Interference-Plus-Noise Ratio
<b>SINDR</b>	signal-to-interference-noise-and-distortion ratios
<b>SNDR</b>	Signal-to-Noise-and-Distortion Ratio
<b>SNR</b>	Signal-to-Noise Ratio
<b>SR</b>	Secondary Receiver
<b>SSC</b>	Spectrum Sharing Cooperation
<b>ST</b>	Secondary Transmitter
<b>SU</b>	Secondary User
<b>SWIPT</b>	Simultaneous Wireless Information Power Transfer
<b>TS</b>	Time-Switching

# CHAPTER 1

## INTRODUCTION

Over the years, there has been an evolution in wireless communication, starting from the late 19th century's first wireless telegraphy systems to modern wireless fidelity (Wi-Fi) technologies and cellular networks. Nowadays, wireless communication finds its use in several applications, including but not limited to smart homes, remote healthcare, autonomous vehicles, laptops, tablets, and mobile phones.

Modern wireless networks must be installed in order to handle the rapidly increasing data traffic caused by the proliferation of the ubiquity of mobile apps and their incorporation into various aspects of our everyday routines. The progression of communication technology has moved beyond its initial stages, starting from first-generation (1G) and now advancing up to sixth-generation (6G) [1]. To build the succeeding generation of communication networks, several crucial aspects must be considered, such as high-speed internet access, extensive capacity, reduced signal latency, prolonged battery life, and broader coverage.

The objective of the Internet of Things (IoT) is to facilitate the seamless and extensive linking of multiple physical objects and sensor nodes. This will enable the implementation of several remote sensing and intelligent city applications. To support these applications, there is a need for the development of advanced wireless networks such as 6G and beyond 6G that can facilitate event monitoring, data collection, and information exchange between IoT devices. Given the rapid proliferation of IoT devices and the growing demand for high-data-rate services, the development and deployment of 6G systems must tackle two significant challenges: scarcity of spectrum and energy limitations. The current licensed band communications may not be adequate for accommodating a large volume of devices in 6G networks that

enable IoT connectivity.

Allowing IoT devices to function in the license-free band could remove the necessity for a dedicated spectrum, but this could also lead to notable interference from other applications sharing the same spectrum.

The lifespan of the IoT network is restricted due to the finite capacity of batteries used in smart sensor devices. Hence, enhancing energy efficiency is crucial to minimize energy demands and prolong the duration of IoT networks.

## 1.1 Cognitive Radio

The utilization of limited spectrum resources in wireless communication can be greatly improved by cognitive radio (CR), which has the potential to revolutionize the industry. Additionally, cognitive radio can increase the efficiency of wireless communication, reduce interference, and enhance the quality of service for end-users. There are three fundamental forms of CR, namely overlay, underlay, and interweave paradigms [2].

**Interweave Approach:** The interweave technique involves secondary users (SUs) accessing primary user's (PU's) vacant spectrum, also known as white spaces, without disrupting their transmission. One significant disadvantage of this approach is that SUs rely on accurate spectrum sensing and primary traffic behavior detection, which makes them highly vulnerable to errors. This approach may not be suitable for dense networks due to a shortage of available spectrum holes.

**Underlay Approach:** CR devices with underlay capabilities possess sophisticated sensing and interference suppression methods that allow them to identify the existence of primary users and either refrain from utilizing their frequency bands or lessen their transmission power as needed. Collecting the channel state information (CSI) of the relevant links to the PUs is necessary for the SUs to adjust their transmission power. The limited power at SUs makes improving their performance crucial but challenging in this paradigm. [9]

**Overlay Approach:** Under this approach, SUs might be authorized to utilize PUs' frequency range in return for aiding the PUs to transmit their messages with higher priority. overlay cognitive radio (O-CR) systems offer the benefit of enhancing spectrum utilization without causing any disturbance to the already-existing primary systems. Nevertheless, O-CR systems confront various difficulties, includ-

ing the requirement for precise spectrum detection, the possibility of interfering with primary systems, and the need for cooperation between primary and secondary systems. Hence, continuous research is underway to enhance and streamline O-CR systems for feasible deployment [30].

The overlay framework, unlike the underlay model, doesn't impose strict transmission power restrictions on SUs.

## 1.2 Cooperative Relaying

Cooperative relaying has been identified as an effective approach to combat the impacts of multipath fading in wireless communication. This technique can be broadly categorized into fixed relaying and adaptive relaying.

### 1.2.1 Fixed Relaying

In this relaying scheme, the resources of the channel are allocated in a predetermined manner between the source and the relay.

Although easy to construct, these protocols suffer from low bandwidth efficiency.

Amplify-and-forward (AF) and decode-and-forward (DF) techniques are commonly used in fixed relaying.

**Amplify-and-Forward Relaying:** The AF relaying protocol operates by having the relay amplify the signal from the source and transmit it to the destination without processing. Its primary goal is to combat fading between the source and relay channels. Nevertheless, the protocol's critical drawback is the relay's ability to amplify noise. On the other hand, the AF protocol's less complex hardware offers some benefits when compared to its DF counterpart. [41]

**Decode-and-Forward Relaying:** DF relaying is also referred to as regenerative relaying. In DF relaying, the signal is decoded by the relay upon reception from the source, re-encoded, and then transmitted to the target. Decoding and relaying an incorrect signal may result in errors that can render the decoding process ineffective.

## 1.3 Non-Orthogonal Multiple Access

To meet the demands for high connectivity and spectral efficiency (SE), it is crucial for forthcoming wireless networks to be efficient. A potential solution for the next generation of wireless networks is the implementation of non-orthogonal multiple

access (NOMA) systems [12]. The underlying concept of NOMA involves serving multiple users concurrently by utilizing the same time or frequency band while assigning distinct power levels to each user. The desired signals are subsequently decoded using the successive interference cancellation (SIC) process at the destination end [35]. To provide a spatial diversity boost for the NOMA user who is far away and has a bad connection, the cooperative relaying approach has been added to the original NOMA scheme in the interim. This method is known as cooperative NOMA (C-NOMA) [36].

## 1.4 Unmanned Aerial Vehicles

In the past few years, the use of drones, or unmanned aerial vehicles (UAVs), has gained significant popularity across numerous applications, one of which is wireless communication [38]. These drones can act as aerial base stations, enhancing communication in areas where traditional infrastructure is inadequate or unavailable.

- Equipped with wireless communication devices, UAVs can offer a variety of services, including internet connectivity, real-time video streaming, and communication for disaster management. The use of UAVs in wireless communication has several benefits, such as coverage in remote areas, flexibility, and quick deployment.
- However, the limited flight time and range of UAVs pose a significant challenge in using them for wireless communication. To address this issue, researchers are working on new technologies, such as advanced battery technologies and energy-efficient communication protocols, to increase UAV flight time [37].
- The potential to transform communication through the deployment of UAVs in wireless networks is considerable, particularly in areas where traditional communication infrastructure is inadequate or non-existent.

## 1.5 System Imperfections

A communication system's performance can be affected by limitations or constraints, which are known as system imperfections. These imperfections can stem from a range of factors, including hardware limitations, environmental conditions, or design

choices. Typically, imperfections can be categorized into three primary groups: channel imperfections, hardware imperfections, and algorithmic imperfections.

1. **Channel Imperfections:** The channel is used to transport information between the source and receiver, which is not ideal due to various constraints and external factors. Consequently, the quality of the system may be influenced by the imperfections present in the channel, such as interference, noise, and fading.
2. **Hardware Imperfections:** Hardware imperfections in a communication system are caused by limitations of the physical components used, such as electronic components, power amplifiers, filters, and antennas. Nonlinear distortion, and frequency offset, are some examples of common hardware imperfections that can occur due to these factors.
3. **Algorithmic Imperfections:** Algorithmic imperfections in communication systems pertain to the constraints of signal processing algorithms utilized. These imperfections may arise from factors such as subpar algorithmic performance, deficient parameter estimation, or design preferences. Channel estimation errors, timing errors, and power allocation errors are among the frequently encountered types of algorithmic imperfections.

In conclusion, system imperfections can arise due to various factors, and their impact on the system performance can be significant. Understanding and mitigating these imperfections is critical to achieving optimal performance in communication systems.

## 1.6 Background Works

A promising method to control the rapidly expanding number of mobile applications over the finite spectrum is CR [8]. It can significantly increase the SE of wireless networks using the interweave, underlay, and overlay paradigms of spectrum access. The underlay and overlay models are two distinct approaches employed in wireless communication scenarios to ensure coexistence between primary and secondary users to permit simultaneous data transmissions of PUs and SUs by operating over the same frequency band and satisfying the quality of service (QoS) constraint for the PU, the system can function without relying on spectrum sensing and opportunistic spectrum access, as opposed to the interweave model. When the interference

constraint for the PU is met, the SU is allowed to transmit data using an underlay technique [9] in the direction of its destination. Conversely, in an overlay model, the SU focuses on assisting the PU's communication by engaging in relay cooperation, thereby gaining access to the PU's licensed spectrum [10], [11]. NOMA enables the multiplexing of multiple users in the power domain, allowing them to transmit over the same time/frequency band. This is in contrast to orthogonal multiple access (OMA). To do this, it uses SIC, which demultiplexes the superimposed signals at the receiver, in conjunction with superposition coding at the transmitter [12]. Eventually, the cognitive NOMA approach, which integrates NOMA with CR, has shown to be a potential method for improving SE in future wireless networks [13]. Numerous studies have investigated cognitive NOMA systems that incorporate the underlay approach and overlay approach [14], [15], [17], [18]. The authors investigated and NOMA has been explored for large-scale underlay CR networks in [14], and used a stochastic geometry approach to examine the outage probability (OP) performance. Furthermore, a DF [15] relaying protocol was used to assess the OP measure of SUs in underlay cognitive NOMA relay networks. In contrast to the underlay cognitive NOMA model, the overlay model utilizes the secondary transmitter (ST) as a relay for the PU while simultaneously implementing the NOMA principle to enable communication with the secondary receivers (SRs) [16], [17]. In [18], to facilitate spectrum sharing, an overlay approach employing NOMA was utilized to serve numerous PUs over an integrated satellite-terrestrial network. It should be highlighted that the overlay NOMA model might eliminate the interference temperature constraint ensures that the interference generated by the ST to the primary receiver (PR) remains within acceptable limits, and thereby, it can improve the OP performance of the PU through ST (relay) as a means of cooperative diversity advantage.

The deployment of energy harvesting (EH) in CR networks holds significant promise, development aiming to increase energy efficiency and SE. Energy-limited SUs will be more able to sustain themselves since they can share the spectrum and gather energy from nearby radio-frequency (RF) sources. Several studies have used simultaneous wireless information power transfer (SWIPT) in cognitive NOMA systems [19]-[23]. Authors in [19], specifically proposed a novel strong NOMA user acts as an EH relay and helps a weak NOMA user by implementing a power-splitting

(PS) scheme in the cooperative multiple-input single-output SWIPT NOMA protocol. The research in [20], examined a secondary network's secure energy efficiency maximization problem while also examining a NOMA cognitive underlay system. The authors of [21], investigated a CR system where the ST uses the RF signal to gather energy from the primary transmitter (PT). The ST sends its data utilizing downlink NOMA and serves as the primary system's DF relaying service. In this study, the outage performance of cooperative CR networks with SWIPT [22], where the cognitive relay uses the PS method to obtain transmission power from the ST, and the NOMA protocol uses the fixed power allocation scheme. In some additional studies, a full-duplex ST was chosen to convey the PT information for IoT network across a cognitive relay that uses the PS method to obtain transmission power from the ST [23].

Recent research has shown that deep learning (DL) approaches are useful for addressing a number of real-world problems in today's wireless communication networks, including resource allocation, congestion control, and queue management [24]. Deep neural network (DNN) was utilised to determine, a cell-edge user's productivity under both perfect SIC (pSIC) and imperfect SIC (iSIC) [25] for CR powered by wireless-IoT relay networks using NOMA. In [26], in order to solve classification and regression issues in cognitive two-way relaying networks, a DNN was built, particularly for the purpose of relay selection. In [27], authors have studied a DNN incorporated into a NOMA system and showed off its impressive channel encoding, decoding, and detection capabilities. Authors in [28], have presented a novel approach to optimizing service distribution in IoT networks, which uses deep learning to learn the optimal distribution strategy.

## 1.7 Motivation and Objectives

In this section, we present the motivation and objectives behind the research work in this thesis.

### 1.7.1 Motivation

Previous studies have suggested the use of pSIC and high-quality RF transceivers to evaluate SWIPT-enabled cognitive NOMA networks. However, implementing pSIC is challenging, and RF transceivers are susceptible to hardware impairments, such

as amplifier non-linearities, phase imbalances, and phase noises. As IoT networks are expected to have numerous connections, inexpensive devices may need to be incorporated, which can also cause HIs. While compensation algorithms can mitigate some HIs, residual impairments may persist in practical applications.

Design objectives such as SE, seamless data communication, and wide coverage are essential considerations for upcoming wireless networks, including 5G and 6G. To address the under-utilization of spectrum, the promising CR technology can be utilized to enhance SE. By incorporating CR techniques into NOMA, the efficiency of future wireless networks can be greatly improved. The fusion of NOMA into CR networks is referred to as cognitive radio NOMA (CR-NOMA).

The previously mentioned studies have shown that the improvement in the performance of the OP comes with a trade-off in spectrum efficiency, as a half-duplex (HD) relay cooperation mode requires more time resources.

The capacity of the SWIPT-based cognitive NOMA system may be limited by iSIC and HIs, especially for high data rate applications. Previous studies have examined the effects of iSIC on cognitive NOMA networks, but not in the context of SWIPT. Additionally, previous research on cooperative NOMA-based IoT networks with RF-EH has not considered dynamic CR networks, which offer greater functionality. No research has yet analyzed the performance of cognitive NOMA systems with SWIPT, considering the combined impacts of iSIC and HIs. Understanding the effects of iSIC and HIs on cognitive NOMA IoT networks, that uses the EH method is crucial for sustainable communication in 6G environments.

UAVs are now commonly used as wireless access platforms for reliable communication. Advancements in drone technology have made affordable, robust, and small UAVs possible. Therefore, UAV-assisted wireless communication is expected to be a potential contender for IoT-inspired 6G networks.

### 1.7.2 Objectives

The aforementioned research voids have motivated us to achieve the following objectives towards the design of future wireless networks: The major objectives are as follows:

- To evaluate the effectiveness of IoT-inspired cooperative spectrum sharing transmission (I-CSST) scheme using primary direct transmission scheme (PDT) as a benchmark.

- To compare the performance of I-CSST using NOMA and OMA technique. We further highlighted the performance advantages of I-CSST with NOMA over OMA.
- To examine the performance of I-CSST scheme in the presence of different fading environments by considering the effect of HIs at transceiver and iSIC at the receiver.
- To provide a NOMA-based power allocation strategy, with the help of the generated OP expressions.
- To determine data-based solution using DNN analysis and to compare the DNN analysis with mathematical analysis and Monte-Carlo simulation to illustrate how long it takes to execute an OP prediction.

## 1.8 Contributions

As a result of the previous discussion, we assess the effectiveness of an overlay cognitive NOMA (OC-NOMA) system, in this study, we consider the effects of iSIC and HIs on the involved devices. SU node, which typically lacks a distinct spectrum for communication, could be the affordable energy-constrained components in small cell IoT networks. We consider a case where a PT and its PR are in downlink contact with the aid of a secondary network made up of a single ST-SR pair. In addition, ST is presumptively equipped with RF-based EH unit on a UAV. Additionally, it can use a shared spectrum for its own transmission while acting as a DF relay for main communications. The ST relays the main signal and transmits its own signal at the same time, splitting the power it has captured into two halves in accordance with the NOMA principle. The following are the thesis's main contributions.

- We propose an EH-based I-CSST scheme for the OC-NOMA system employing UAV-assisted DF relaying strategy. We also explore the PDT scheme as a benchmark for evaluating the I-CSST's effectiveness for the OC-NOMA system under consideration. We further illustrate the relative performance advantages of I-CSST with NOMA compared to OMA.
- Using the received signal-to-noise-and-distortion ratios (SNDRs) and signal-to-interference-noise-and-distortion ratios (SINDRs), we thoroughly examine the

accurate and asymptotic OP performance of the I-CSST schemes for primary and secondary IoT networks in the presence of HIs and iSIC over heterogeneous Rician and Nakagami- $m$  fading environments.

- With the help of the generated OP expressions, we provide a NOMA-based power allocation strategy, and evaluate the system throughput and energy efficiency to become aware of the OC-NOMA system.
- It is difficult to examine the OP for UAV-borne OC-NOMA systems because of their complex derivations. This creates a substantial hurdle for the model-based approach, therefore in order to achieve realistic real-time OC-NOMA network setups, we construct a DNN model as an unique data-driven alternative for OP prediction with high accuracy and low latency. The implementation time and root-mean-square error (RMSE) are the key metrics for evaluating the effectiveness and precision of our design method when predicting the performance of complicated network circumstances.

## 1.9 Organization of the Thesis

- Chapter-1 encompasses an overview of wireless communication and the technologies utilized in this field such as CR, NOMA, UAV, Cooperative Relaying, and their respective applications.
- Chapter-2 includes system descriptions and performance analysis. The primary network's OP performance analysis using the PDT and I-CSST schemes is presented. Additionally, the performance analysis of the secondary network is also carried out in this chapter.
- Chapter-3 includes DNN design, dataset generation technique, DNN architecture and real-time prediction of OP.
- Chapter-4 provides numerical and simulation investigation. It includes OP performance of the primary network, OP performance of the secondary network, OP performance comparison of NOMA with OMA, throughput plots for OC-NOMA system, and energy efficiency plots for OC-NOMA system.
- Chapter-5 presents a summary and conclusion of the research work, including in-depth discussions based on the obtained results. This chapter also explores

the potential for future work within the scope of the study. Additionally, the appendices provide the proof of useful theorems and lemmas.

## CHAPTER 2

# SYSTEM DESCRIPTIONS AND PERFORMANCE

## ANALYSIS

The increasing amount of mobile data traffic motivates researchers to look into communication systems that are both spectral-efficient and energy-efficient strategies in 6G wireless networks [1]. In order to meet customer demands in the near future, the limited amount of spectrum that is now accessible must be used effectively [2]. The need for high data transfer speeds, improvements in QoS, connecting massive equipment, etc., has aggravated this situation. Beyond SE, energy efficiency has also emerged as a crucial issue for designing future IoT networks [3], [4]. When the devices are distantly located and lack a regular power source, the increasing concern lies in the growing significance of energy consumption. SWIPT technology allows wireless devices to process information and capture energy from surrounding RF signals at the same time. By doing so, it aims to address these issues [5]. For SWIPT realization, two schemes are prevalent: TS and PS [6]. In SWIPT using PS, a fraction of the received power is assigned for EH, while the remaining power is employed for information processing (IP). In contrast, TS-based SWIPT divides time between EH and IP stages in an alternating manner [7].

*Notations:* An intricate Gaussian distribution with a mean of Zero and variance of  $\sigma^2$  is denoted as  $\mathcal{CN}(0, \sigma^2)$ . For a random variable  $X$ , the cumulative distribution function (CDF) and probability density function (PDF) are abbreviated, respectively, by  $f_X(\cdot)$  and  $F_X(\cdot)$ . Further,  $\mathcal{K}_v(\cdot)$  is the modified Bessel function of the second kind as stated in [39, eq. 8.432.6], while  $\Gamma(\cdot)$  and  $\Upsilon(\cdot, \cdot)$  are the lower, incomplete Gamma function, and the full Gamma function, respectively, as stated in [39, eqs. (8.310.1) and (8.350.1)].  $\mathbb{E}[\cdot]$  stands for expectancy, and  $\binom{p}{q} = \frac{p!}{q!(p-q)!}$  be the coefficient of the binomial.

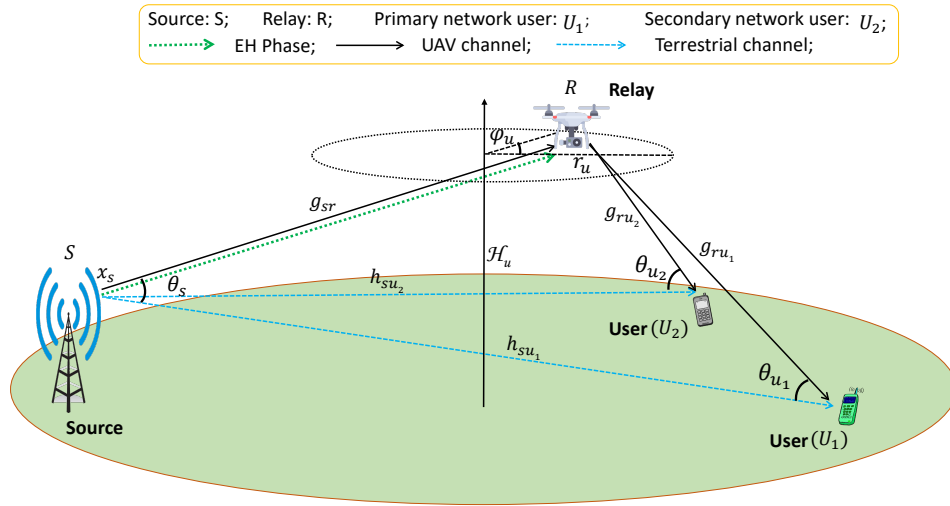


Figure 2.1: OC-NOMA system model.

## 2.1 System Model and I-CSST Scheme Description

In this chapter, we describe the concerned OC-NOMA system and channel models, and explain the proposed EH-based I-CSST scheme using DF relaying strategy.

### 2.1.1 System and Channel Models

We consider an OC-NOMA system as shown in Fig. 2.1, which consists of a primary source ( $S$ ), a secondary source ( $R$ ) which also acts as a relay, and two users viz., a PU ( $U_1$ ) and a SU ( $U_2$ ). Herein, the primary source  $S$  transmits its message signal to the  $U_1$  with the help of the relay  $R$  which is deployed over a UAV. As such, we take into account a UAV-aided system in which the UAV converses with two NOMA users, i.e.,  $U_1$  and  $U_2$ . The UAV flies at an altitude of  $h$ , a constant velocity of  $v$ , and a circular trajectory of  $r$ . Even though main channel has been allotted between  $S$  and  $U_1$ , the  $S$  might still approach the adjacent  $R$  for assistance and harnessing a diversity advantage. In exchange, the  $R$  can use the primary's authorized spectrum for its own transmission to the  $U_2$ . The  $S$  is regarded as having a reliable power source feeding it, and broadcasts its signal at a constant transmit power. As the  $R$  being assumed as an energy-constrained node, it harvests energy from the RF signals transmitted by the primary source  $S$ . In anticipation of helping with the primary transmission between the  $S$  and  $U_1$ , the  $R$  is given access to the licensed primary spectrum based on an overlay paradigm. For this,  $R$  serves as a cooperative relay

and uses the NOMA approach to concurrently transmit its own signal to the SU and help forward the primary source's signal to the PU. To examine the underlying I-CSST scheme for the OC-NOMA system under consideration, as explained in the sequel, we here utilize a PS-based EH technique.

The coordinates of ground nodes  $S$ ,  $U_1$ , and  $U_2$  in three-dimensional (3-D) Cartesian space are denoted by  $\mathbf{v}_s = (\mathcal{X}_s, \mathcal{Y}_s, 0)$ ,  $\mathbf{v}_{u_1} = (\mathcal{X}_{u_1}, \mathcal{Y}_{u_1}, 0)$ , and  $\mathbf{v}_{u_2} = (\mathcal{X}_{u_2}, \mathcal{Y}_{u_2}, 0)$ , respectively. It is expected that the UAV will follow a circular trajectory with radius  $r_u$ , height  $\mathcal{H}_u$  so that  $\mathcal{H}_u \in [\mathcal{H}_u^{\min}, \mathcal{H}_u^{\max}]$ , and constant speed, where  $\mathcal{H}_u^{\min}$  and  $\mathcal{H}_u^{\max}$  are the minimum and maximum allowed heights, respectively. Let  $\varphi_u$  represent the angle the UAV is presently positioned at, with respect to the  $x$ -axis within the UAV circle. As a result,  $\mathbf{v}_u = (r_u \cos \varphi_u, r_u \sin \varphi_u, \mathcal{H}_u)$  can be used to indicate the UAV's location. The locations of  $S$ ,  $U_j$ , and the UAV can be denoted by the two-dimensional (2-D) cartesian coordinates  $\mathbf{w}_s = (\mathcal{X}_s, \mathcal{Y}_s)$ ,  $\mathbf{w}_{u_j} = (\mathcal{X}_{u_j}, \mathcal{Y}_{u_j})$ , and  $\mathbf{w}_u = (r_u \cos \varphi_u, r_u \sin \varphi_u)$ , respectively. Let  $\theta_s = \arctan\left(\frac{\mathcal{H}_u}{|\mathbf{w}_u - \mathbf{w}_s|}\right)$  and  $\theta_{u_j} = \arctan\left(\frac{\mathcal{H}_u}{|\mathbf{w}_u - \mathbf{w}_{u_j}|}\right)$ , with  $j \in \{1, 2\}$ , provide the elevation angles (in rad) between  $S$  and the UAV and between users and the UAV, respectively.

We have assumed that all the nodes use single-antenna devices and operate in a HD mode. Additionally, the devices have cheaper RF transceiver components installed, which accounts for their HIs. Since it is believed that every channel would adhere to the block fading, they will all stay the same for the duration of the block, but may vary on their own during the transmission over the different blocks. We have given independent Nakagami- $m$  fading [30] for the communication links from  $S$  to  $U_1$  and  $U_2$  with the channel coefficients  $h_{su_1}$  and  $h_{su_2}$ , respectively. The squared channel gain  $|h_{ij}|^2$  follows the Gamma distribution with an average power of  $\Omega_{ij}$  and a fading severity parameter of  $m_{ij}$ , for  $i \in \{s\}$  and  $j \in \{u_1, u_2\}$ , with  $i \neq j$ . As a result, the corresponding PDF and CDF expressions of  $|h_{ij}|^2$  can be obtained by

$$f_{|h_{ij}|^2}(z) = \frac{1}{\Gamma(m_{ij})} \left(\frac{m_{ij}}{\Omega_{ij}}\right)^{m_{ij}} (z)^{m_{ij}-1} e^{-\left(\frac{m_{ij}}{\Omega_{ij}}\right)z}, \quad (2.1)$$

and

$$F_{|h_{ij}|^2}(z) = \frac{1}{\Gamma(m_{ij})} \Upsilon\left(m_{ij}, \left(\frac{m_{ij}}{\Omega_{ij}}\right)z\right). \quad (2.2)$$

Once the path-loss model is taken into account, we obtain  $\Omega_{ij} = d_{ij}^{-\alpha_{ij}}$ , where  $d_{ij}$  is

the normalised distance between nodes  $i$  and  $j$  and  $\alpha_{ij}$  is the path-loss exponent. As a result, since the propagation energy decreases at the rate of  $d_{ij}^{-\alpha_{ij}}$ , the RF energy in the RF-based EH system could be harvested at very low power density. The additive white Gaussian noise (AWGN) with zero mean and variance  $\sigma^2$  also has an impact on all receiving nodes.

In accordance with the elevation angle and surroundings, the terrestrial node and UAV communication channels ( $S$ ,  $U_1$ , and  $U_2$ ) may have line-of-sight (LoS) or non-LoS. As a result, the probability of LoS in their relevant links is provided by

$$P_L(\theta_j) = \left(1 + \varepsilon_j \exp(-\xi_j(\theta_j - \varepsilon_j))\right)^{-1}, \quad (2.3)$$

where  $\varepsilon_j$  and  $\xi_j$ , with  $j \in \{s, u_1, \text{ and } u_2\}$ , the environment parameters obtained from the curve fitting using the Damped Least-Squares (DLS) approach should be denoted [40]. The corresponding path-loss exponent is given by

$$\alpha_{r,j}(\theta_j) = P_L(\theta_j)\kappa_j + \nu_j, \quad (2.4)$$

where  $\kappa_j$  and  $\nu_j$ , with  $\varepsilon_j$  and  $\xi_j$ , for  $j \in \{s, u_1, \text{ and } u_2\}$ , represent constants that depend on the uplink and downlink environment [40]. The link between  $S$  and  $R$  is separated by  $d_{sr} = \sqrt{|\mathbf{w}_u - \mathbf{w}_s|^2 + \mathcal{H}_u^2}$ , and the link between  $R$  and  $U_k$  is separated by  $d_{ru_k} = \sqrt{|\mathbf{w}_u - \mathbf{w}_{u_k}|^2 + \mathcal{H}_u^2}$ . The related aerial path-loss exponents are  $\alpha_{r,s}(\theta_s)$  and  $\alpha_{r,u_k}(\theta_{u_k})$ , respectively. Likewise, we assume that  $d_{su_k} = |\mathbf{w}_s - \mathbf{w}_{u_k}|$  and  $\alpha_{su_k}$ , where  $k \in \{1, 2\}$ , are the distance and path-loss exponent, respectively, for the corresponding terrestrial channel.

The channel between UAV and ground nodes ( $S$ ,  $U_1$ , or  $U_2$ ) is typically characterised by a strong LoS path. In order to deal with LoS and multipath scatterers at the ground receiver, the independent Rician fading is applied to the channel between UAV and ground nodes, whereby the channel coefficients for the links  $S$ - $R$ ,  $R$ - $U_1$ , and  $R$ - $U_2$  being represented by  $g_{sr}$ ,  $g_{ru_1}$ , and  $g_{ru_2}$ , respectively. In order to depict the PDF and CDF of the channel gain  $|g_{ij}|^2$ , for  $i \in \{s, r\}$  and  $j \in \{r, u_1, u_2\}$ , with

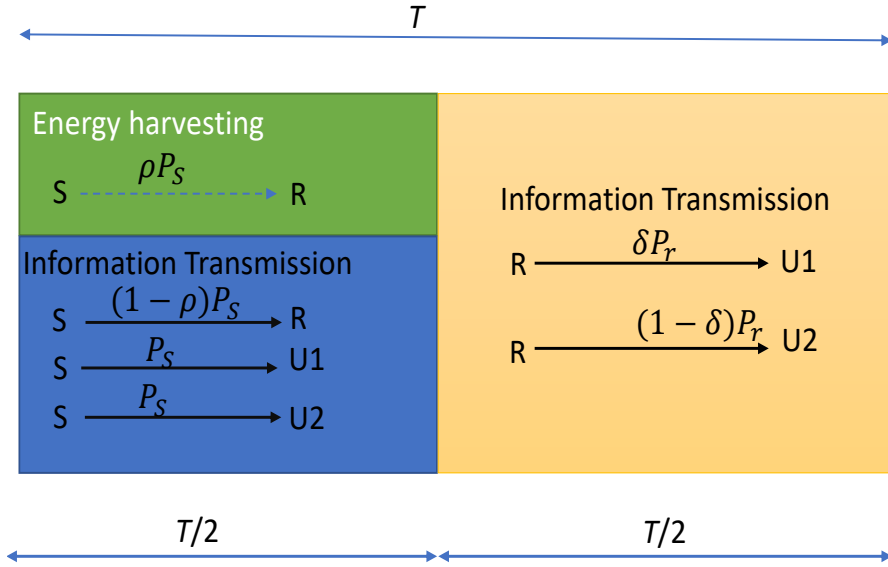


Figure 2.2: Transmission block structure for the PS-based EH.

$i \neq j$ , a non-central, two-degrees-of-freedom chi-square distribution is utilised as

$$\begin{aligned}
 f_{|g_{ij}|^2}(z) &= b_{ij} e^{-K_{ij}} e^{-b_{ij}z} I_0\left(2\sqrt{K_{ij} b_{ij} z}\right) \\
 &= e^{-K_{ij}} e^{-b_{ij}z} \sum_{l=0}^{\infty} \frac{K_{ij}^l b_{ij}^{k+1}}{l! \Gamma(l+1)} z^l
 \end{aligned} \tag{2.5}$$

and

$$F_{|g_{ij}|^2}(z) = 1 - Q\left(\sqrt{2K_{ij}}, \sqrt{2b_{ij}z}\right), \tag{2.6}$$

where  $b_{ij} = (K_{ij} + 1) / \Omega_{ij}$ , with  $K_{ij} \triangleq |\mu_{ij}|^2 / 2\sigma^2$ ,  $\Omega_{ij} = d_{ij}^{-\alpha_{ij}}$ ,  $I_0(z)$ , and  $Q(a, b)$  representing the first-order modified Bessel function in the zeroth order, the Rician factor, the normalised average fading power, and the Marcum Q-function of the first-order, respectively.

### 2.1.2 PS-Based EH with Source Transmission

In the considered system, an energy harvester is used by the UAV to generate electricity for data transmission and spectrum sensing. It should be noted that in our study, the energy that is harvested is mostly used for sensing and transmission, while the embedded battery of the UAV is primarily responsible for providing the energy required for UAV flying, hovering, and other expenses. Due to the HD operation employed in the PS-based EH, the block transmission time  $T$  is split

into two sub-blocks, with one half being utilised for primary transmission (first transmission phase) and the other for secondary transmission (second transmission phase), as illustrated in Fig. 2.2. Node  $S$  transmits a unit-power signal  $x_s$  during the first transmission phase, and as a result, the signals received at nodes  $U_1$  and  $U_2$  can be represented by  $y_{su_1}$  and  $y_{su_2}$ , respectively, and expressed as

$$y_{sj} = h_{sj} \left( \sqrt{P_s} x_s + \eta_{ts} \right) + \eta_{rsj} + \Psi_{sj}, \quad (2.7)$$

where  $j \in \{u_1, u_2\}$ , transmit power at  $S$  is denoted as  $P_s$ , the distortion noise for transmit processing at  $S$  is represented by  $\eta_{ts} \sim \mathcal{CN}(0, \lambda_{ts}^2 P_s)$ , the distortion noise for receive processing at the  $j$ -th node is represented by  $\eta_{rsj} \sim \mathcal{CN}(0, \lambda_{rsj}^2 P_s |h_{sj}|^2)$ , where  $\lambda_{ts}$  and  $\lambda_{rsj}$  represent the severity of the impairments such that  $\lambda_{sj} = \sqrt{\lambda_{ts}^2 + \lambda_{rsj}^2}$ , and  $\Psi_{sj}$  represents the AWGN variable. Consequently, the final SNDR at  $j$ -th node,  $j \in \{u_1, u_2\}$ , via the direct transmission (DT)-link, can be represented as

$$\gamma_{sj}^{\text{DT}} = \frac{\Delta_s |h_{sj}|^2}{\Delta_s |h_{sj}|^2 \lambda_{sj}^2 + 1}, \quad (2.8)$$

where  $\Delta_s = \frac{P_s}{\sigma^2}$  be the transmit signal-to-noise ratio (SNR) at node  $S$ . The received signal at  $R$  is given as

$$y_{sr} = g_{sr} \left( \sqrt{P_s} x_s + \eta_{ts} \right) + \eta_{rsr} + \Psi_{sr}, \quad (2.9)$$

where  $\eta_{rsr} \sim \mathcal{CN}(0, \lambda_{rsr}^2 P_s |g_{sr}|^2)$ . Through the use of the PS-based EH parameter  $\rho$  ( $0 \leq \rho \leq 1$ ), the  $R$  divides the received signal  $y_{sr}$  into two parts. In particular,  $\sqrt{\rho} y_{sr}$  is used to gather energy to refuel its battery, and  $\sqrt{1-\rho} y_{sr}$  is utilised to analyse information. Consequently, the received signal at the energy harvester's input is provided by

$$\sqrt{\rho} y_{sr} = \sqrt{\rho} g_{sr} \left( \sqrt{P_s} x_s + \eta_{ts} \right) + \sqrt{\rho} \eta_{rsr} + \sqrt{\rho} \Psi_{sr}. \quad (2.10)$$

The energy that  $R$  has harvested can be stated using (2.10), as follows:

$$E_r = \frac{\Theta \rho P_s |g_{sr}|^2 T}{2}, \quad (2.11)$$

where  $0 \leq \Theta \leq 1$  is the inverter circuitry's energy conversion efficiency at  $R$ , and the noise statistic [21] is ignored because we were aiming for harvested energy with  $P_r \ll P_s$ . The power will be used for the remaining  $T/2$  time and will therefore be provided by

$$P_r = \frac{E_r}{T/2} = \Theta \rho P_s |g_{sr}|^2 = \beta P_s |g_{sr}|^2, \quad (2.12)$$

where  $\beta = \Theta \rho$ . Contrarily, the base-band signal that the information receiver (IR) at  $R$  has received is represented by

$$\begin{aligned} y'_{sr} &= \sqrt{(1-\rho)} y_{sr} \\ &= \sqrt{1-\rho} g_{sr} \left( \sqrt{P_s} x_s + \eta_{ts} \right) + \sqrt{1-\rho} \eta_{rst} \\ &\quad + \sqrt{1-\rho} \Psi_{sr} + \Psi_{RF}, \end{aligned} \quad (2.13)$$

where  $\Psi_{RF}$  denotes the sample AWGN owing to RF to baseband signal conversion. Consequently, the overall AWGN noise at IR is  $\Psi_{sr} = \sqrt{1-\rho} \Psi_{sr} + \Psi_{RF}$ . As a result, the resulting SNDR through the DT-link at node  $R$  can be expressed as

$$\gamma_{sr}^{\text{DT}} = \frac{(1-\rho)\Delta_s |g_{sr}|^2}{(1-\rho)\Delta_s |g_{sr}|^2 \lambda_{sr}^2 + 1}, \quad (2.14)$$

where  $\lambda_{sr} = \sqrt{\lambda_{ts}^2 + \lambda_{rst}^2}$ .

The DF relaying with OC-NOMA transmission using PS-based EH protocol is described in the next section, and thereby, the users  $U_1$  and  $U_2$ 's corresponding SINDR expressions are obtained.

### 2.1.3 DF Relaying with OC-NOMA Transmission

Here,  $R$  implements a DF-based relaying strategy during the second transmission phase and hence first decodes the primary signal  $x_s$ . If  $R$  is successful in decoding, it applies the NOMA principle to combine the decoded signal  $x_s$  with its own signal  $x_r$  to produce a superimposed signal  $z_r^{\text{DF}}$ . Consequently, the  $R$  node's transmit signal is provided by

$$z_r^{\text{DF}} = \sqrt{\delta P_r} x_s + \sqrt{(1-\delta) P_r} x_r + \eta_{tr}, \quad (2.15)$$

where the transmit power at  $R$  is denoted as  $P_r$ , and the distortion noise for transmit processing at  $R$  is represented by  $\eta_{tr} \sim \mathcal{CN}(0, \lambda_{tr}^2 P_r)$ . Following that, the corresponding signals obtained at  $U_1$  and  $U_2$  from  $R$  can be represented by  $y_{ru_1}^{\text{DF}}$  and  $y_{ru_2}^{\text{DF}}$ , being provided as

$$y_{rj}^{\text{DF}} = g_{rj} z_r^{\text{DF}} + \eta_{rrj} + \Psi_{rj}, \quad (2.16)$$

for  $j \in \{u_1, u_2\}$ . Herein, the distortion noise for receive processing at the  $j$ -th node is represented by  $\eta_{rrj} \sim \mathcal{CN}(0, \lambda_{rrj}^2 P_r |g_{rj}|^2)$ , with  $\lambda_{tr}$  and  $\lambda_{rrj}$  being the severity of the impairments such that  $\lambda_{rj} = \sqrt{\lambda_{tr}^2 + \lambda_{rrj}^2}$ , and  $\Psi_{rj}$  represents the AWGN variable. The SNDR expression at  $U_1$ , based on (2.15) and (2.16), can be stated as

$$\gamma_{ru_1}^{\text{DF}} = \frac{\delta \beta \Delta_s |g_{sr}|^2 |g_{ru_1}|^2}{\beta \Delta_s |g_{sr}|^2 |g_{ru_1}|^2 \Xi_p + 1}, \quad (2.17)$$

where  $\Xi_p = (1 - \delta) + \lambda_{ru_1}^2$  with  $\lambda_{ru_1} = \sqrt{\lambda_{tu_1}^2 + \lambda_{rru_1}^2}$ . The  $U_1$  now exploits MRC to combine the source's signal components received in first transmission phase (via DT) and in second transmission phase, subject to the source's signal being successfully decoded at  $R$  (via relay transmission).

The  $U_2$  implements SIC in accordance with the NOMA principle. The  $U_2$  accomplishes this by first decoding the source's signal  $x_s$ , removing  $x_s$  from  $y_{ru_2}^{\text{DF}}$ , and then decoding its own signal  $x_r$ . The  $U_2$  first decodes source's signal, while considering the signal  $R$ 's as noise. In light of (2.15) and (2.16), the resulting SINDR expression at  $U_2$  can be stated as

$$\gamma_{ru_2 \rightarrow x_s}^{\text{DF}} = \frac{\delta \beta \Delta_s |g_{sr}|^2 |g_{ru_2}|^2}{\beta \Delta_s |g_{sr}|^2 |g_{ru_2}|^2 \Xi_s + 1}, \quad (2.18)$$

where  $\Xi_s = (1 - \delta) + \lambda_{ru_2}^2$  with  $\lambda_{ru_2} = \sqrt{\lambda_{tr}^2 + \lambda_{rru_2}^2}$ . Remembering that  $U_2$  picks up the source's signal in the first transmission phase, it is now possible for it to use the MRC to decode  $x_s$  during the SIC process.  $U_2$  can then decode  $x_s$  and take it out of the  $y_{ru_2}$  received NOMA signal. When taking into account the iSIC scenario, the SINDR at  $U_2$  can be written as

$$\gamma_{ru_2}^{\text{DF}} = \frac{(1 - \delta) \beta \Delta_s |g_{sr}|^2 |g_{ru_2}|^2}{\beta \Delta_s |g_{sr}|^2 (\lambda_{ru_2}^2 |g_{ru_2}|^2 + \delta |h_I|^2) + 1}, \quad (2.19)$$

where  $h_I$  is the residual interference signal (IS) [23] channel coefficient at  $U_2$  and is subject to Nakagami- $m$  fading with fading severity  $m_I$  and average power  $\mathbb{E}[|h_I|^2] = \xi\Omega_I$ . Herein,  $\xi$  ( $0 \leq \xi \leq 1$ ) accounts for the level of residual IS due to iSIC, i.e.,  $\xi = 0$  implies the case of pSIC.

Again, if decoding of the signal  $x_s$  at  $R$  in the first transmission phase is unsuccessful, it will not communicate during the second transmission phase. In this scenario,  $U_1$  only receives  $x_s$  from the  $S$  over the DT-link during the first transmission phase.

## 2.2 Performance Analysis of Primary Network

In this part, we analyse the accurate and asymptotic OP performance for the primary network using the PDT and I-CSST schemes. We also look at retrieving the NOMA power allocation parameter's effective value.

### 2.2.1 Accurate OP Analysis

#### PDT Scheme

We now take into consideration that PDT just delivers communication through a DT-link only, with no involvement from UAV-borne relay cooperation. We use this scheme as a benchmark to assess the effectiveness of the suggested I-CSST scheme. The OP of the primary network utilising the PDT scheme for a pre-defined target rate  $r_{th}^p$  can be given, by realising that PDT occurs for a single transmission phase, as

$$P_{\text{Pri}}^{\text{PDT}}(r_{th}^p) = \Pr \left[ \log_2 (1 + \gamma_{su_1}^{\text{DT}}) < r_{th}^p \right]. \quad (2.20)$$

Then, (2.20) can be re-expressed as

$$P_{\text{Pri}}^{\text{PDT}}(r_{th}^p) = \Pr \left[ \gamma_{su_1}^{\text{DT}} < \tau_p' \right] = F_{\gamma_{su_1}^{\text{DT}}}(\tau_p'), \quad (2.21)$$

where  $\tau_p' = 2^{r_{th}^p} - 1$ . The CDF in (2.21) can be represented using (2.8) as

$$F_{\gamma_{su_1}^{\text{DT}}}(\tau_p') = \Pr \left[ |h_{su_1}|^2 < \frac{\tau_p'}{\Delta_s (1 - \lambda_{su_1}^2 \tau_p')} \right], \quad (2.22)$$

and can be computed, with the condition on threshold  $\tau'_p$ , as

$$F_{\gamma_{su_1}^{\text{DT}}}(\tau'_p) = \begin{cases} F_{\gamma_{su_1}} \left( \frac{\tau'_p}{\Delta_s(1-\lambda_{su_1}^2 \tau'_p)} \right), & \text{if } \tau'_p < \frac{1}{\lambda_{su_1}^2}, \\ 1, & \text{if } \tau'_p \geq \frac{1}{\lambda_{su_1}^2}. \end{cases} \quad (2.23)$$

This allows for the computation of the required OP by applying (2.2) into (2.23). Note that, starting with (2.23), PDT induces an outage whenever the threshold  $\tau'_p$  exceeds the value  $\frac{1}{\lambda_{su_1}^2}$ .

### I-CSST Scheme

Now, as described in Section 2.1, we examine the OP performance of the I-CSST scheme for the primary network. The primary network's OP formulation under the I-CSST scheme can be given by considering the target rate  $r_{th}^p$  as

$$P_{\text{Pri}}^{\text{CSST}}(r_{th}^p) = \Pr[\gamma_{sr}^{\text{DT}} \geq \tau_p, (\gamma_{su_1}^{\text{DT}} + \gamma_{ru_1}^{\text{DF}}) < \tau_p] \\ + \Pr[\gamma_{sr}^{\text{DT}} < \tau_p, \gamma_{su_1}^{\text{DT}} < \tau_p], \quad (2.24)$$

where  $\tau_p = 2^{2r_{th}^p} - 1$ . The OP expression in (2.24) can be further expressed as

$$P_{\text{Pri}}^{\text{CSST}}(r_{th}^p) = \left(1 - F_{\gamma_{sr}^{\text{DT}}}(\tau_p)\right) \underbrace{\Pr[(\gamma_{su_1}^{\text{DT}} + \gamma_{ru_1}^{\text{DF}}) < \tau_p]}_{P_1} \\ + F_{\gamma_{sr}^{\text{DT}}}(\tau_p) F_{\gamma_{su_1}^{\text{DT}}}(\tau_p). \quad (2.25)$$

We must evaluate the CDF  $F_{\gamma_{sr}^{\text{DT}}}(\tau_p)$  and the probability term  $P_1$  in order to calculate (2.25). Using (2.14), it is possible to extract the CDF  $F_{\gamma_{sr}^{\text{DT}}}(\tau_p)$  as

$$F_{\gamma_{sr}^{\text{DT}}}(\tau_p) = \begin{cases} F_{\gamma_{sr}} \left( \frac{\tau_p}{(1-\rho)\Delta_s(1-\lambda_{sr}^2 \tau_p)} \right), & \text{if } \tau_p < \frac{1}{\lambda_{sr}^2}, \\ 1, & \text{if } \tau_p \geq \frac{1}{\lambda_{sr}^2}. \end{cases} \quad (2.26)$$

Next,  $P_1$  can be evaluated as

$$P_1 = \int_0^{\tau_p} \left( \int_0^{\tau_p - y} f_{\gamma_{ru_1}^{\text{DF}}}(x) dx \right) f_{\gamma_{su_1}^{\text{DT}}}(y) dy \\ = \int_0^{\tau_p} \left( F_{\gamma_{ru_1}^{\text{DF}}}(\tau_p - y) \right) f_{\gamma_{su_1}^{\text{DT}}}(y) dy. \quad (2.27)$$

In order to calculate (2.27), one needs the CDF  $F_{\gamma_{ru_1}^{DF}}(\cdot)$ , which can be determined by using (2.17) as in the following lemma.

**Lemma 1.** *The Rician fading can be applied to determine the CDF  $F_{\gamma_{ru_1}^{DF}}(w)$  for the I-CSST scheme in the OC-NOMA system as*

$$F_{\gamma_{ru_1}^{DF}}(w) = \begin{cases} \mathbb{A}_1(w) - \mathbb{A}_2(w), & \text{if } w < \frac{\delta}{\Xi_p}, \\ 0, & \text{if } w \geq \frac{\delta}{\Xi_p}, \end{cases} \quad (2.28)$$

where  $\mathbb{A}_1(w)$  and  $\mathbb{A}_2(w)$  are, respectively, given as

$$\mathbb{A}_1(w) = \sum_{l=0}^{\infty} \sum_{f=0}^{\infty} \left( \frac{(K_{ru_1})^{l+f}}{(l!)(f!)} \right) e^{-2K_{ru_1}} \quad (2.29)$$

and

$$\begin{aligned} \mathbb{A}_2(w) &= \sum_{l=0}^{\infty} \sum_{a=0}^l \sum_{n=0}^{\infty} \left( \frac{(K_{ru_1})^{l+n} (b_{ru_1})^{a+n+1}}{(l!)(a!)(n!)^2} \right) (T_1)^{\frac{a+n+1}{2}} \\ &\times e^{-2K_{ru_1}} \mathcal{K}_{n-a+1} \left( 2\sqrt{T_1 b_{ru_1}^2} \right), \end{aligned} \quad (2.30)$$

with  $T_1 = \frac{w}{\beta \Delta_s (\delta - \Xi_p w)}$ .

*Proof.* See Appendix A. ■

Furthermore, by using the expression of  $F_{\gamma_{ru_1}^{DF}}(w)$  from (2.28) and inserting the PDF expression of  $\gamma_{su_1}^{DT}$  into (2.27), it is realised that a closed-form solution for  $P_1$  would be intractable. Therefore, we apply an  $L$ -stairways conjecture [41] to simplify  $P_1$  as for the complicated integral sector in (2.27) to obtain

$$\begin{aligned} P_1 &\approx \sum_{n=0}^{L-1} \left\{ F_{\gamma_{su_1}^{DT}} \left( \frac{n+1}{L} \tau_p \right) - F_{\gamma_{su_1}^{DT}} \left( \frac{n}{L} \tau_p \right) \right\} \\ &\times F_{\gamma_{ru_1}^{DF}} \left( \frac{L-n}{L} \tau_p \right). \end{aligned} \quad (2.31)$$

Finally,  $P_{\text{Pri}}^{\text{CSST}}(r_{th}^p)$  can be evaluated by inserting the CDF expressions from (2.23) and (2.28) into (2.31) and the resulting expression together with (2.23) and (2.26) into (2.25).

## 2.2.2 Asymptotic OP Analysis

In order to determine the diversity order, we achieve an asymptotic OP expression in (2.25) for high SNR ( $\Delta_s, \Delta_r \rightarrow \infty$ ). In the beginning, we exploit the fact that the lower incomplete gamma function  $\Upsilon(a, z)$  [39, eq. 8.354.1] can be approximated as

$$\Upsilon(a, z) = \sum_{n=0}^{\infty} \frac{(-1)^n z^{a+n}}{n! (a+n)} \underset{z \rightarrow 0}{\approx} \left( \frac{z^a}{a} \right). \quad (2.32)$$

At high SNR, we are able to alter CDF from (2.2) as

$$F_{|h_{ij}|^2}(z) \approx \frac{1}{\Gamma(m_{ij} + 1)} \left( \frac{m_{ij}}{\Omega_{ij}} z \right)^{m_{ij}}. \quad (2.33)$$

It follows that the PDT scheme's asymptotic OP can be expressed as

$$\begin{aligned} P_{\text{Pri}}^{\text{PDT, asy}}(r_{th}^p) &= F_{\gamma_{su_1}^{\text{DPT}}}^{\text{asy}}(\tau_p') \\ &= \frac{1}{\Gamma(m_{su_1} + 1)} \left( \frac{m_{su_1} T_2}{\Omega_{su_1}} \right)^{m_{su_1}}, \end{aligned} \quad (2.34)$$

where  $T_2 = \frac{\tau_p'}{\Delta_s(1-\lambda_{su_1}^2 \tau_p')}$ . The asymptotic OP for the primary network's I-CSST scheme can be further assessed as

$$\begin{aligned} P_{\text{Pri}}^{\text{CSST, asy}}(r_{th}^p) &= \left( 1 - F_{\gamma_{sr}^{\text{DPT}}}^{\text{asy}}(\tau_p) \right) \underbrace{\Pr[(\gamma_{su_1}^{\text{DPT}} + \gamma_{ru_1}^{\text{DF}}) < \tau_p]}_{P_1^{\text{asy}}} \\ &\quad + F_{\gamma_{sr}^{\text{DPT}}}^{\text{asy}}(\tau_p) F_{\gamma_{su_1}^{\text{DPT}}}^{\text{asy}}(\tau_p). \end{aligned} \quad (2.35)$$

Asymptotic expressions of the relevant CDFs and the probability term are computed for the evaluation of (2.35) as follows.

Under Rician fading, the CDF  $F_{\gamma_{sr}^{\text{DPT}}}^{\text{asy}}(\tau_p)$  for I-CSST system can be stated as

$$F_{\gamma_{sr}^{\text{DPT}}}^{\text{asy}}(\tau_p) = \sum_{l=0}^{\infty} \frac{(K_{sr})^l (b_{sr} T_3)^{l+1}}{(l!)^2 (l+1)} e^{-K_{sr}}, \quad (2.36)$$

where  $T_3 = \frac{\tau_p}{(1-\rho)\Delta_s(1-\lambda_{sr}^2 \tau_p)}$  for  $\tau_p < \frac{1}{\lambda_{sr}^2}$ .

The CDF  $F_{\gamma_{ru_1}^{\text{DF}}}^{\text{asy}}(\tau_p)$  can be calculated, similar to condition like (2.28), as

$$F_{\gamma_{ru_1}^{\text{DF}}}^{\text{asy}}(\tau_p) = \sum_{l=0}^{\infty} \sum_{f=0}^{\infty} \frac{(K_{ru_1} b_{ru_1})^{l+f} (b_{ru_1})^{l-f+2} (T_1)^{(l+1)}}{(l!)^2 (f!)^2 (l+1)} \times (f-l-1)! e^{(-2K_{ru_1})}, \quad (2.37)$$

for  $\tau_p < \frac{\delta}{\Xi_p}$ . Next,  $P_1^{\text{asy}}$  in (2.35) can be evaluated, similar to condition (2.31), as

$$P_1^{\text{asy}} \approx \sum_{n=0}^{L-1} \left\{ F_{\gamma_{su_1}^{\text{DT}}}^{\text{asy}}\left(\frac{n+1}{L} \tau_p\right) - F_{\gamma_{su_1}^{\text{DT}}}^{\text{asy}}\left(\frac{n}{L} \tau_p\right) \right\} \times F_{\gamma_{ru_1}^{\text{DF}}}^{\text{asy}}\left(\frac{L-n}{L} \tau_p\right). \quad (2.38)$$

Finally,  $P_{\text{Pri}}^{\text{CSST, asy}}(r_{th}^p)$  can be evaluated by inserting the CDF expressions from (2.34) and (2.37) into (2.38) and the resulting expression together with (2.34) and (2.36) into (2.35). Thus, on applying [42]  $d_{\text{Pri}}^{\text{DT}} = -\lim_{\Delta_s \rightarrow \infty} \frac{\log(P_{\text{Pri}}^{\text{DT, asy}}(\Delta_s))}{\log(\Delta_s)}$  and  $d_{\text{Pri}}^{\text{CSST}} = -\lim_{\Delta_s \rightarrow \infty} \frac{\log(P_{\text{Pri}}^{\text{CSST, asy}}(\Delta_s))}{\log(\Delta_s)}$ , the primary network's diversity orders for PDT and I-CSST schemes are  $d_{\text{Pri}}^{\text{DT}} = m_{su_1}$  and  $d_{\text{Pri}}^{\text{CSST}} = m_{su_1} + 1$ , respectively.

### 2.2.3 NOMA Power Allocation Parameter

To create the NOMA power allocation policy for  $R$ , it is necessary to keep in mind that the QoS criterion for the primary network must be met. To keep the primary network's QoS intact, we actually need to choose an appropriate value for the NOMA power allocation parameter  $\delta$ . As such, from (2.28), iterating the conditions  $\tau_p < \frac{\delta}{\Xi_p}$ , the permissible range of  $\delta$  for a given threshold  $\tau_p$  can be calculated as  $\frac{\tau_p(1+\lambda_{ru_1}^2)}{1+\tau_p} < \delta < 1$  for the I-CSST scheme. An important point to note is that a lower value of  $\delta$  can provide the secondary communication additional NOMA power, increasing the potential for spectrum access. However,  $U_1$  being a NOMA user with a high priority, a higher value of  $\delta$  is allocated correspondingly to  $U_1$ .

## 2.3 Performance Analysis of Secondary Network

Here, we provide an accurate and asymptotic OP analysis of the secondary network for the I-CSST enabled OC-NOMA system by taking into account the two SIC situations viz., iSIC and pSIC.

### 2.3.1 Accurate OP Analysis

For a target rate of  $r_{th}^s$ , the OP formulation for the secondary network under the I-CSST scheme can be expressed as

$$P_{Sec}^{CSST}(r_{th}^s) = \Pr[\gamma_{sr}^{DT} \geq \tau_p] \underbrace{\left(1 - \Pr[\gamma_{u_2}^{MRC} \geq \tau_p, \gamma_{ru_2}^{DF} \geq \tau_s]\right)}_{P_2} + \Pr[\gamma_{sr}^{DT} < \tau_p], \quad (2.39)$$

where  $\tau_s = 2^{r_{th}^s} - 1$ . We can evaluate (2.39) further as

$$P_{Sec}^{CSST}(r_{th}^s) = [1 - F_{\gamma_{sr}^{DT}}(\tau_p)](1 - P_2) + F_{\gamma_{sr}^{DT}}(\tau_p). \quad (2.40)$$

The joint probability term  $P_2$  needs to be calculated to evaluate (2.40). It is deduced in the next subsections for the iSIC and pSIC situations.

#### iSIC

In the subsequent theorem, we derive the expression of  $P_2$  for the instance of iSIC.

**Theorem 1.** *The probability term  $P_2$  in (2.40) can be calculated under iSIC situation as*

$$P_2 = \begin{cases} P_{21} \times P_{22}, & \text{if } \tau_p > \frac{\delta}{\Xi_s}, \\ P_{22}, & \text{if } \tau_p \leq \frac{\delta}{\Xi_s}, \end{cases} \quad (2.41)$$

with

$$P_{21} \approx 1 - \sum_{n=0}^{L-1} \left\{ F_{\gamma_{su_2}^{DT}}\left(\frac{n+1}{L}\tau_p\right) - F_{\gamma_{su_2}^{DT}}\left(\frac{n}{L}\tau_p\right) \right\} \times F_{\gamma_{ru_2, x_s}^{DF}}\left(\frac{L-n}{L}\tau_p\right) \quad (2.42)$$

and

$$P_{22} = \begin{cases} \mathbb{C}_1(\tau_s) - \mathbb{C}_2(\tau_s), & \text{if } \tau_s < \frac{1-\delta}{\lambda_{ru_2}^2}, \\ 0, & \text{if } \tau_s \geq \frac{1-\delta}{\lambda_{ru_2}^2}, \end{cases} \quad (2.43)$$

where

$$\begin{aligned} \mathbb{C}_1(\tau_s) &= \sum_{l=0}^{\infty} \sum_{f=0}^{\infty} \sum_{b=0}^f \sum_{p=0}^{\infty} \frac{(K_{ru_2}^{l+f+p}) (b_{ru_2}^{b+p+1})}{(l!)(f!)(b!)(p!)^2} (b+p)! \\ &\quad \times \left(\frac{T_6}{T_5}\right)^b \left(\frac{b_{ru_2} T_6}{T_5} + b_{ru_2}\right)^{-(b+p+1)} e^{-3K_{ru_2}}, \end{aligned} \quad (2.44)$$

and

$$\begin{aligned} \mathbb{C}_2(\tau_s) &= \sum_{l=0}^{\infty} \sum_{a=0}^l \sum_{n=0}^{\infty} \sum_{c=0}^n \sum_{q=0}^{\infty} \frac{(K_{ru_2}^{l+n+q}) (b_{ru_2}^{a+n+q+2})}{(l!)(a!)(n!)^2(q!)^2} \\ &\quad \times (n-c+q)! \binom{n}{c} \left(\frac{\tau_s}{T_4}\right)^a \left(\frac{T_6}{T_5}\right)^{n-c} (T_5)^{-(c+1)} \\ &\quad \times \left(\frac{b_{ru_2} T_6}{T_5} + b_{ru_2}\right)^{-(n-c+q+1)} e^{-3K_{ru_2}}, \end{aligned} \quad (2.45)$$

with  $T_4 = \beta\Delta_s$ ,  $T_5 = (1-\delta) - \lambda_{ru_2}^2 \tau_s$ , and  $T_6 = \delta\tau_s$ .

*Proof.* See Appendix B. ■

The relevant CDFs in (2.42) can be easily determined similar to (2.23) and (2.28). The appropriate OP expression for the secondary network can be obtained by putting the results from (2.26) and (2.41) into (2.40).

### P-SIC

In this scenario,  $P_{22}$  can be used to calculate the OP of the secondary network while using  $k_2 = 0$ .

$$P_{22} = \begin{cases} \mathbb{D}_1(\tau_s) - \mathbb{D}_2(\tau_s), & \text{if } \tau_s < \frac{1-\delta}{\lambda_{ru_2}^2}, \\ 0, & \text{if } \tau_s \geq \frac{1-\delta}{\lambda_{ru_2}^2}, \end{cases} \quad (2.46)$$

where

$$\mathbb{D}_1(\tau_s) = \sum_{l=0}^{\infty} \sum_{f=0}^{\infty} \frac{K_{ru_2}^{l+f}}{(l!)(f!)} e^{(-2K_{ru_2})}, \quad (2.47)$$

$$\mathbb{D}_2(\tau_s) = \sum_{l=0}^{\infty} \sum_{a=0}^l \sum_{n=0}^{\infty} \frac{(K_{ru_2})^{l+n} (b_{ru_2})^{a+n+1}}{(l!)(a!)(n!)^2} (T_7)^a e^{(-2K_{ru_2})}, \quad (2.48)$$

where  $T_7 = \frac{\tau_s}{\beta \Delta_s [(1-\delta) - \lambda_{ru_2}^2 \tau_s]}$ . Now, on inserting (2.46) into (2.41) and the result along with (2.26) into (2.40), one can fetch the requisite OP expression.

### 2.3.2 Asymptotic OP Analysis

The secondary network's asymptotic OP can be determined using the formula

$$P_{\text{Sec}}^{\text{CSST, asy}}(r_{\text{th}}^s) = [1 - F_{\gamma_{sr}^{\text{DT}}}^{\text{asy}}(\tau_p)](1 - P_2^{\text{asy}}) + F_{\gamma_{sr}^{\text{DT}}}^{\text{asy}}(\tau_p). \quad (2.49)$$

To evaluate (2.49), we need to obtain the expression of the joint probability term  $P_2^{\text{asy}}$ . We derive it in the next subsections for the iSIC and pSIC situations.

#### iSIC

For the case of iSIC, we derive the expression of  $P_2^{\text{asy}}$  as

$$P_2^{\text{asy}} = \begin{cases} P_{21}^{\text{asy}} \times P_{22}^{\text{asy}}, & \text{if } \tau_p > \frac{\delta}{\Xi_s}, \\ P_{22}^{\text{asy}}, & \text{if } \tau_p \leq \frac{\delta}{\Xi_s}, \end{cases} \quad (2.50)$$

with

$$P_{21}^{\text{asy}} \approx 1 - \sum_{n=0}^{L-1} \left\{ F_{\gamma_{su_2}^{\text{DT}}}^{\text{asy}}\left(\frac{n+1}{L} \tau_p\right) - F_{\gamma_{su_2}^{\text{DT}}}^{\text{asy}}\left(\frac{n}{L} \tau_p\right) \right\} \\ \times F_{\gamma_{ru_2, xs}^{\text{DF}}}^{\text{asy}}\left(\frac{L-n}{L} \tau_p\right) \quad (2.51)$$

and probability term  $P_{22}^{\text{asy}}$  in (2.50) can be evaluated as

$$P_{22}^{\text{asy}} = \sum_{l=0}^{\infty} \sum_{f=0}^{\infty} \sum_{a=0}^f \sum_{n=0}^{\infty} \frac{(K_{ru_2})^{l+f+n} (b_{ru_2})^{l+f+n+3}}{(l!)^2 (f!)^2 (n!)^2 (l+1)} e^{-3K_{ru_2}} \\ \times \left(\frac{\tau_s}{T_4}\right)^{l+1} (T_5)^{-(f+1)} (T_6)^{(f-a)} \left(\frac{b_{ru_2}}{T_5}\right)^{-(a-l)} \binom{f}{a} \\ \times (a-l-1)! (f-a+n)! \left(\frac{b_{ru_2} T_6}{T_5} + b_{ru_2}\right)^{-(f-a+n+1)}. \quad (2.52)$$

The relevant CDFs in (2.51) can be determined similar to (2.34) and (2.37). The appropriate OP expression for the secondary network can be obtained by putting the results from (2.36) and (2.50) into (2.49). Hereby, we examine the diversity order  $d_{\text{Sec}}^{\text{iSIC}} = -\lim_{\Delta_s \rightarrow \infty} \frac{\log(P_{\text{Sec}}^{\text{CSST, asy}}(\Delta_s))}{\log(\Delta_s)}$  to illustrate that  $d_{\text{Sec}}^{\text{iSIC}} = 0$ . The appropriate

OP curves would therefore achieve error ceilings in the high SNR area.

### P-SIC

In this scenario,  $P_{22}^{\text{asy}}$  can be used to calculate the OP of the secondary network while using  $k_2 = 0$  as

$$P_{22}^{\text{asy}} = \sum_{l=0}^{\infty} \sum_{f=0}^{\infty} \frac{(K_{ru_2})^{l+f} (b_{ru_2})^{2(l+1)}}{(l!)^2 (f!)^2 (l+1)} (f-l-1)! \times (T_7)^{l+1} e^{-(2K_{ru_2})}. \quad (2.53)$$

Now, on inserting (2.53) into (2.50) and the result along with (2.36) into (2.49), one can fetch the requisite OP expression. Hereby, we examine the diversity order  $d_{\text{Sec}}^{\text{pSIC}} = -\lim_{\Delta_s \rightarrow \infty} \frac{\log(P_{\text{Sec}}^{\text{CSST, asy}}(\Delta_s))}{\log(\Delta_s)}$  to illustrate that  $d_{\text{Sec}}^{\text{pSIC}} = 0$ . As a result, the corresponding OP curves would attain error floors in the high SNR region.

## 2.4 Overall OC-NOMA System Performance

Based on the advancements in earlier parts, we examine the throughput and energy efficiency performance for the entire OC-NOMA system employing I-CSST scheme in this section.

### 2.4.1 System Throughput

For the OC-NOMA system under consideration, the system throughput is a critical performance indicator to evaluate spectrum usage. It indicates the average SE for wireless networks using cooperative communication [23]. The sum of the separate target rates for the primary and secondary communications that can be successfully achieved can be used to quantify it attained via the Rician and Nakagami- $m$  fading channels for the proposed OC-NOMA system. The deduced OP expressions for both primary and secondary networks allow us to derive the system throughput for the I-CSST scheme as

$$\mathcal{S}_T^{\text{CSST}} = \left[ (1 - P_{\text{Pri}}^{\text{CSST}}(r_{th}^p)) r_{th}^p + (1 - P_{\text{Sec}}^{\text{CSST}}(r_{th}^s)) r_{th}^s \right]. \quad (2.54)$$

When  $r_{th}^p = r_{th}^s = \mathfrak{R}$  is used, the maximum system throughput for the I-CSST scheme is  $\mathfrak{R}$ , which could be achieved under optimal hardware and pSIC circumstances under a high SNR environment.

### 2.4.2 Energy Efficiency

We can examine the energy efficiency of the EH-based OC-NOMA system under I-CSST scheme by using the throughput equations in (2.54). Such a study implies that it can assist in designing an EH-aware OC-NOMA system to increase network lifetime. Fundamentally, the system's energy efficiency is defined as the ratio between the amount of provided data and the amount of energy used [23]. As stated in (2.54), the system throughput for the I-CSST scheme implies the total amount of data provided. In contrast, with the PS-based EH method in the I-CSST scheme, the total energy spent in the system equals the sum of the energy used by the source during the EH phase (which lasts for  $T/2$  of time) and its use during the first transmission phase ( $T/2$  of time). Notably, the energy used in the second transmission phase is the energy obtained by relay in the EH phase and does not contribute to the system's overall energy consumption. As a result, the energy efficiency for the OC-NOMA system under consideration, using I-CSST scheme, can be represented as

$$\mathcal{E}^{\text{CSST}} = \frac{\mathcal{S}_T^{\text{CSST}}}{\frac{\Delta_s}{2}}, \quad (2.55)$$

where  $\mathcal{S}_T^{\text{CSST}}$  in bps/Hz is given in (2.54).



This chapter encompasses several important aspects, such as the design of DNN, techniques for generating datasets, the architecture of DNN, and the real-time prediction of OP. A DNN is a highly effective model for machine learning. It is composed of interconnected nodes or artificial neurons arranged in multiple layers. These nodes analyze and modify input data, enabling the network to understand intricate patterns and connections within the data. DNN demonstrates exceptional capabilities in areas like image and speech recognition, natural language processing, and decision-making. They leverage algorithms to adapt the weights, which represent connections between neurons, by comparing predicted outputs to actual outputs. This iterative process gradually enhances their performance. The process of designing a DNN encompasses several critical factors, encompassing the selection of architecture, configuration of layers, implementation of activation functions, utilization of optimization algorithms, application of regularization techniques, and data preprocessing. Developing a robust and efficient model for a particular task necessitates expertise in the field, along with experimentation and continuous improvement. Ongoing advancements in deep learning research consistently expand the capabilities of deep neural networks, establishing them as vital instruments within contemporary machine learning applications.

### 3.1 Deep Neural Network Design

To address the challenges of mathematical analysis and Monte-Carlo simulations, we propose the utilization of the DNN framework as an alternative approach for estimating the OP. This method offers the advantage of reduced computing complexity

and faster run time. As the calculation of OP depends on various parameters as listed in Table I, we can train a neural network to learn this relationship.

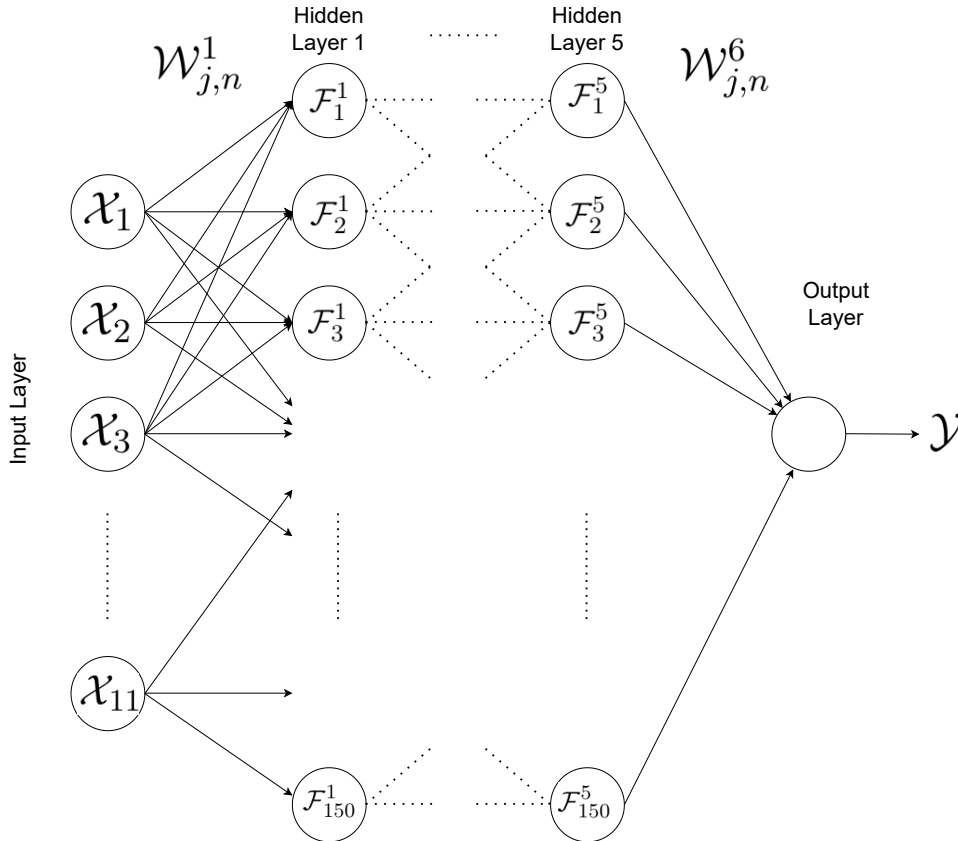


Figure 3.1: DNN deployment architecture.

### 3.1.1 Dataset Generation Technique

We use a DNN to model the regression problem of predicting the OP for various system conditions. The dataset for this study is constructed using the OP expressions provided in (2.24) and (2.39). The calculation of OP depends on various parameters such as SNR ( $\Delta_s$ ), HIs level ( $\lambda_0$ ), power factor ( $\delta$ ), target rates ( $r_{\text{th}}^p = r_{\text{th}}^s$ ), level of residual interference ( $\Omega_I$ ), radius of UAV ( $r_u$ ), height of UAV ( $\mathcal{H}_u$ ), angular motion of UAV ( $\varphi_u$ ), locations of source ( $\mathcal{X}_s, \mathcal{Y}_s, \mathcal{Z}_s$ ), location of  $U_1(\mathcal{X}_{u_1}, \mathcal{Y}_{u_1}, \mathcal{Z}_{u_1})$ , and location of  $U_2(\mathcal{X}_{u_2}, \mathcal{Y}_{u_2}, \mathcal{Z}_{u_2})$ . Therefore, while constructing the dataset, we should consider different values for each parameter in some defined ranges. The parameters and their ranges are listed in Table 3.1. It is important to note that each system's parameter is uniformly sampled in the provided range and later various combinations of these parameters are used with (2.24) and (2.39) to generate OP values. Specifically, we picked 5 samples for each parameter.

Table 3.1: DNN training and testing input parameters.

Parameters (Input)	Values	Parameters (Input)	Values
$\Delta_s$	$[-10, 40]$	$\lambda_0$	$[0, 0.3]$
$\delta$	$[0.51, 0.99]$	$r_{\text{th}}^p = r_{\text{th}}^s$	$[0.1, 1]$
$\Omega_I$	$[0, -40]$	$r_u$	$[0.1, 20]$
$\mathcal{H}_u$	$[0.1, 35]$	$\varphi_u$	$[0, 2\pi]$
$(\mathcal{X}_s \mathcal{Y}_s \mathcal{Z}_s)$	$[-20 \ 0 \ 20]$	$(\mathcal{X}_{u_1} \mathcal{Y}_{u_1} \mathcal{Z}_{u_1})$	$[20 \ -20 \ 0]$
$(\mathcal{X}_{u_2} \mathcal{Y}_{u_2} \mathcal{Z}_{u_2})$	$[20 \ 0 \ 0]$	—	—

The dataset  $\mathcal{D}$  is composed of row vectors, each of which contains the dataset  $[d]$ . This dataset includes both the feature vector  $\mathcal{X}[d]$  and the simulated output  $\mathcal{Y}^{\text{sim}}$  for a given sample  $d$ . The feature vector  $\mathcal{X}[d]$  is made up of all the input variables specified in Table 3.1. Every feature vector  $\mathcal{X}[d]$  is utilized to build actual OP sets from (2.24) and (2.39), and each one is fed into simulation and given a unique output  $\mathcal{Y}^{\text{sim}}$ . The total number of samples in the created dataset ( $D_s$ ) is  $10^6$ , of which 80% are used for training ( $D_{s,\text{trn}}$ ), and the remaining 20% are split equally between validation ( $D_{s,\text{val}}$ ) and testing ( $D_{s,\text{tes}}$ ). We have come to the conclusion that most of the time, this amount of samples is enough to get estimations that are fairly accurate.

Keep in mind that as there are more samples of each parameters in their considered ranges, more data needs to be generated. This is essential for better training of the DNN in order to get high prediction accuracy.

### 3.1.2 DNN Architecture

Our DNN architecture consists of a feed-forward neural network comprising 1 input layer, 5 hidden layers, each containing 150 neurons, and 1 output layer, as depicted in Fig. 3.1. The eleven parameters given in Section 3.1.1 have corresponding neural counterparts in the eleven input layer neurons. At the output of each neuron in the hidden layers, a threshold operation is performed using an activation function called exponential linear unit (eLU). Values below zero are adjusted to zero through scaling. The eLU is defined mathematically as

$$\text{eLU}(x) = \begin{cases} \varrho(e^x - 1), & x < 0, \\ x, & x \geq 0, \end{cases} \quad (3.1)$$

where  $x$  is the input parameter, the constant  $\varrho$  has the value 1. Due to its almost linear nature, there are several advantages associated with the eLU activation function when compared to other activation functions. As this is a regression problem to predict the OP value, the output layer of our network contains only one neuron without any subsequent modification or activation function. The  $n$ -th neuron in the  $m$ -th layer produces an output denoted as  $\mathcal{F}_n^m$ , which is connected to the outputs of all neurons in the previous  $(m - 1)$ -th layer and is computed as

$$\mathcal{F}_n^m = \text{eLU} \left( \sum_{j=1}^{\mathcal{U}_{m-1}} \mathcal{W}_{j,n}^m \mathcal{F}_j^{m-1} + \mathcal{C}_n^m \right), \quad (3.2)$$

where  $\mathcal{U}_{m-1}$  is the  $(m - 1)$ -th layer's total number of neurons.  $\mathcal{W}_{j,n}^m$  denotes the weight of the link from neuron ( $j$ ) in layer  $(m - 1)$  to neuron ( $n$ ) in layer  $(m)$ , while  $\mathcal{C}_n^m$  denotes the scalar bias in the  $(m)$ -th layer.

### 3.1.3 Real-Time Prediction of OP

Training a DNN requires careful optimization of the weights and biases of the network. We employ the Adam optimization algorithm for this purpose. Adam uses a method of gradient descent to update the network's weights and biases during backpropagation. Further, the accuracy of the network's predictions is measured by the mean squared error (MSE), and this number is used to modify the weights and biases during the optimization process. Let  $\mathcal{Y}^d$  and  $\bar{\mathcal{Y}}^d$  represent the true and predicted outputs of the DNN for a certain training sample  $d$  then the MSE loss of the training phase is calculated as

$$\text{Loss}(\mathcal{Y}^d, \bar{\mathcal{Y}}^d) = \frac{1}{\mathcal{D}_{s,tes}} \sum_{d=1}^{\mathcal{D}_{s,tes}} (\mathcal{Y}^d - \bar{\mathcal{Y}}^d)^2. \quad (3.3)$$

The Adam optimization algorithm is able to adjust the biases and weights of the network to minimize the MSE and maximise the accuracy of the predictions generated by the network.

In the following chapter, we compare the DNN analysis to mathematical analysis and Monte-Carlo simulation to illustrate how long it takes to execute an OP prediction.



## CHAPTER 4

# NUMERICAL AND SIMULATION INVESTIGATION

This chapter presents a comprehensive analysis comprising numerical and simulation investigations. The analysis encompasses the OP performance evaluation of the primary network, as well as the OP performance assessment of the secondary network. Furthermore, a comparative analysis of OP performance between NOMA and OMA is conducted. Additionally, this chapter includes throughput plots illustrating the performance of the OC-NOMA system, as well as energy efficiency plots for the OC-NOMA system.

### 4.1 Numerical and Simulation Results

We perform numerical analysis of the proposed UAV relaying OC-NOMA system and make use of Monte-Carlo simulations in MATLAB version R2022a in order to validate our theoretical aspects. Unless otherwise specified, we set up a few system parameters, which are depicted in Table 4.1. While obtaining the path-loss model,  $\Omega_{ij} = d_{ij}^{-\alpha_{ij}}$ , we utilise a 3-D network configuration. We also set  $\lambda_{ts} = \lambda_{tr} = \lambda_{rsu_1} = \lambda_{rsr} = \lambda_{rsu_2} = \lambda_{rru_1} = \lambda_{rru_2} = \lambda_0$  as the level of HIs such that  $\lambda_{su_1} = \lambda_{sr} = \lambda_{su_2} = \lambda_{ru_1} = \lambda_{ru_2} = \sqrt{2}\lambda_0$ . These parameters are ascertained by the EVMs [43].

Using Python version 3.7.13 in conjunction with Keras 2.8.0 and Tensor-Flow 2.8.0, DNN is constructed with five hidden layers, each containing 150 neurons. Throughout the course of 70 training epochs, to begin the training process of the DNN, its weights are initialized randomly. This is done using the Adam optimizer, with a gradient decay value set to 0.95. It begins with a learning rate of  $10^{-3}$ , which falls to 90% after 20 epochs. All tests are performed on a computer with an i7 – 7700

Table 4.1: Simulation Parameters [with  $j \in \{1, 2\}$ ].

Parameters	Values
Average fading powers ( $\Omega_{su_j}$ )	0.1, 0.1
Fading severity parameters ( $m_{su_j}$ )	1, 1
Average power gain of IS channel ( $\Omega_I$ )	0.1
Rician factor ( $K$ )	1
Environment parameters ( $\varepsilon, \xi$ ) [40]	20, 0.5
Uplink and downlink environment ( $\kappa, \nu$ )	-1.5, 3.5
UAV parameters ( $\varphi_u, r_u, \mathcal{H}_u$ ) [40]	$\pi$ , 20 m, 35 m
Location of Source ( $\mathcal{X}_s, \mathcal{Y}_s, \mathcal{Z}_s$ )	(-20, 0, 20) m
Location of $U_1$ and $U_2$ ( $\mathcal{X}_{u_1}, \mathcal{Y}_{u_1}, \mathcal{Z}_{u_1}$ ), ( $\mathcal{X}_{u_2}, \mathcal{Y}_{u_2}, \mathcal{Z}_{u_2}$ )	(20, -20, 0), (20, 0, 0)m
Path loss exponent ( $\alpha_{su_j}$ )	2.2
Level of HIs [43] ( $\lambda_{su_j} = \lambda_{sr} = \lambda_{ru_j} = \sqrt{2}\lambda_0$ )	$\lambda_0 = 0, 0.3$
PS parameter ( $\rho$ )	0.7
Energy conversion efficiency ( $\Theta$ )	0.75
Block duration ( $T$ )	1 sec
Level of stairways conjecture ( $H$ )	50
Noise variance ( $\sigma^2$ )	-114 dBm/Hz
Bandwidth (BW)	1 MHz

processor, an 8 GB GeForce GTX 1080 GPU, and 16 GB of RAM. It should be emphasized that the DNN prediction results are discovered to be pretty well matched with the simulation and the analytical results produced from the formulations in Section 2.2-2.3 for all the subsequent numerical investigations.

Fig. 4.1 depicts the OP and source transmit power plots for the primary network, using different target rate values ( $r_{th}^p = 0.5$  bps/Hz and  $r_{th}^p = 1$  bps/Hz) for both ideal hardware ( $\lambda_0 = 0$ ) and imperfect hardware ( $\lambda_0 = 0.3$ ). In order to fulfill the I-CSST scheme criteria as stated in Section 2.2.3, we select acceptable values of  $\delta$ . Additionally, for comparison, the OP characteristics are also produced for the PDT scheme. The tight wedgedness of the simulated and analytical graphs across the entire power domain may first be confirmed. The asymptotic curves and the analytical and simulated curves are closely matched in the large power area. Additionally, at the fixed target rate, the OP of the I-CSST approach is significantly lower compared to the PDT approach. It should be noticed that all of the curves for the I-CSST scheme (with the given fading settings) have a greater slope since employing cooperative transmission for the primary network has a diversity benefit. Although the addition of HIs ( $\lambda_0 = 0.3$ ) reduces the primary network's performance,

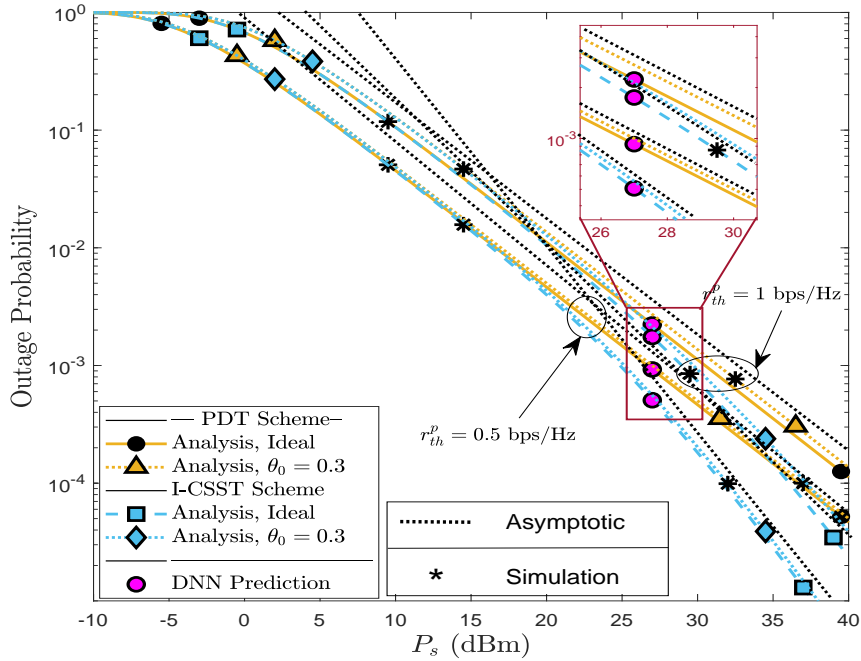


Figure 4.1: OP performance of the primary network.

The impact of the phenomenon becomes more evident as the target rates increase. Additionally, at the high power regime, the HIs have a stronger impact on the I-CSST scheme. Interestingly, as can be noticed, both the DNN prediction and the simulation curves exactly match the analytical calculations given in (2.21) and (2.24).

The OP characteristics of the secondary user in the pSIC and iSIC scenarios is shown in Fig. 4.2. We set the data rate  $r_{th}^p = 0.5$  bps/Hz and  $r_{th}^p = 1$  bps/Hz for both perfect hardware ( $\lambda_0 = 0$ ) and imperfect hardware ( $\lambda_0 = 0.3$ ). To begin with, it is feasible to validate that the simulated and analytical curves exactly matched over the entire range of power. After reaching the high power range, the asymptotic graph match the analytical and simulated curves quite well. With I-CSST scheme, the iSIC scenario has a substantially greater OP than the pSIC case. Additionally, for the iSIC situation, an outage floor happens as a result of the IS channel power gain and associated fading severity parameter. The curves resulting from the I-CSST scheme may be seen to stray more from the ideal curve as the level of HIs increases. As evidence of DNN's superior prediction ability, the results obtained from the DNN prediction exhibit a high degree of similarity with both the analytical and simulation findings.

The performance comparison between the I-CSST scheme based OC-NOMA and OMA system is shown in Fig. 4.3. As shown in the plot,  $U_1$  and  $U_2$  (pSIC) case

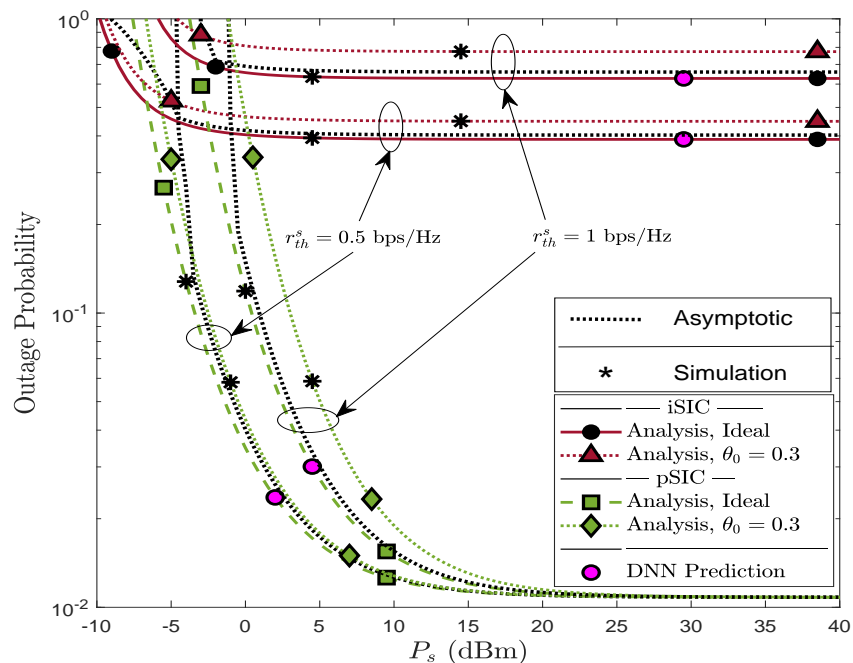


Figure 4.2: OP performance of the secondary network.

of NOMA outperforms OMA significantly for all power values, whereas  $U_2$  (iSIC) case of NOMA outperforms OMA in regions with low power values. It is because of that, OMA system requires three time slots to run, therefore, the corresponding signal-to-interference-plus-noise ratio (SINR) threshold is higher than its NOMA counterpart. While the imposition of HIs ( $\lambda_0 = 0.3$ ) results in a decline in the outage performance of the I-CSST scheme, its effects on the OMA scheme are more noticeable. As a result, it can be concluded that the I-CSST scheme with NOMA is more resistive to HIs than the OMA counterpart.

In order to learn more about the I-CSST scheme for OC-NOMA system's mean SE, In Section 2.4.1, we derived an analytical statement for the system throughput, which we use to generate the curves shown in Fig. 4.4. The figure illustrates how the system throughput changes with the source transmit power for two different target rates. i.e.,  $r_{th}^p = 0.5$  bps/Hz and  $r_{th}^p = 1$  bps/Hz for both ideal hardware ( $\lambda_0 = 0$ ) and imperfect hardware ( $\lambda_0 = 0.3$ ). The pertinent graphs demonstrate that when the goal rate rises, system throughput decreases in the low power zone. The system throughput, in contrast, increases for the stated target rate until a certain power value, at which point it reaches saturation. The greatest throughput that can be achieved for the specified target rate is illuminated as this saturated value. This throughput saturation happens significantly at a high power for higher target rate values. This is because outage performance typically deteriorates as

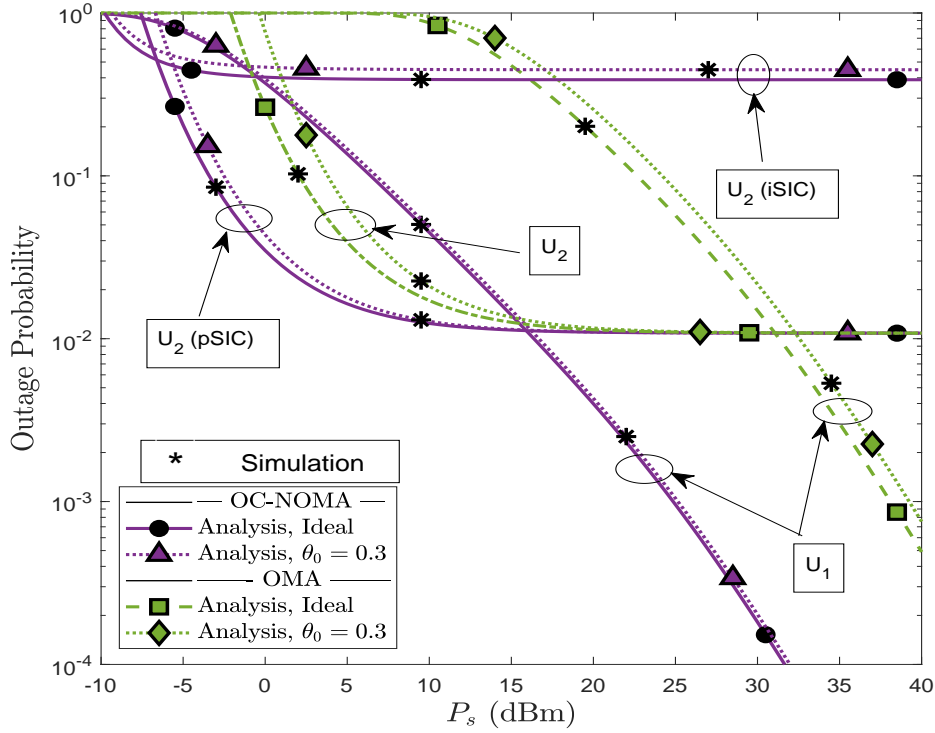


Figure 4.3: OP performance comparison of NOMA with OMA.

the target rate increases, resulting in a worse performance at higher rates than lower ones. Furthermore, it is clear from the two separate HIs values that system throughput declines as HIs levels rise. Additionally, we can also see that the system throughput of the pSIC OC-NOMA system is significantly higher than that of the iSIC OC-NOMA system for the fixed target rate.

Fig. 4.5 sheds light on the OC-NOMA system's energy efficiency. For two different target rates at  $r_{th}^p = 0.5$  bps/Hz and  $r_{th}^p = 1$  bps/Hz under the I-CSST scheme, we create two sets of curves to compare the energy efficiency of the system, one with HIs and one without, plotted against the transmit power of the source. The relevant graphs show that Increasing the target rate has been observed to have a negative impact on the energy efficiency of the system at mid power values. It is clear from looking at two distinct levels of HIs ( $\lambda_0 = 0, 0.3$ ) that, in contrast to the ideal scenario, HIs cause a drop in the system's energy efficiency. This demonstrates that the performance of energy efficiency suffers when HIs are imposed. Furthermore, it is evident from the relevant curves that the optimal level of energy efficiency is achieved by the system during its operation. For a given goal rate and level of HIs at a certain power value. The power value at which the system operates at its most energy-efficient level likewise fluctuates when the desired target rate and amount of

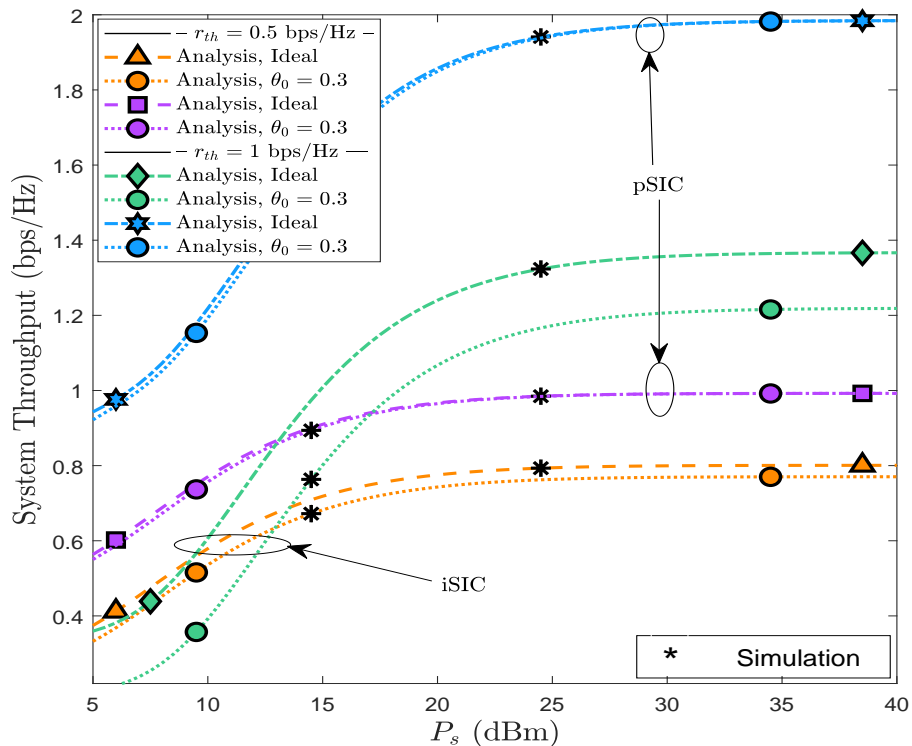


Figure 4.4: Throughput plots for OC-NOMA system.

HIs change. It's important to keep in mind that as the power value increases, the efficiency of the system being analyzed tends to decrease. The main cause of this is increased power consumption compared to system throughput at higher power.

To begin with, we compared the run times for the DNN evaluation, mathematical analysis, and Monte Carlo simulation in our proposed system. Our findings indicate that the DNN prediction method is the fastest, taking only 0.0227 seconds to provide OP values. On the other hand, the Monte Carlo simulation took 7.1965 seconds to obtain the OP values, while the mathematical assessment took 0.0519 seconds.

## 4.2 Summary

We evaluated the effectiveness of an OC-NOMA system using EH-based I-CSST scheme while considering the effects of practically created iSIC and HIs at the transceiver nodes. In particular, we adopted Rician and Nakagami- $m$  fading channels to quantify the total OC-NOMA system performance in terms of system throughput, OP of both users, and energy efficiency. Additionally, our recommendations aim to assist in the appropriate selection of the NOMA power allocation factor to enhance the efficiency of spectrum sharing. It is demonstrated that I-CSST scheme outperforms the benchmark PDT scheme. In particular, it is demonstrated that

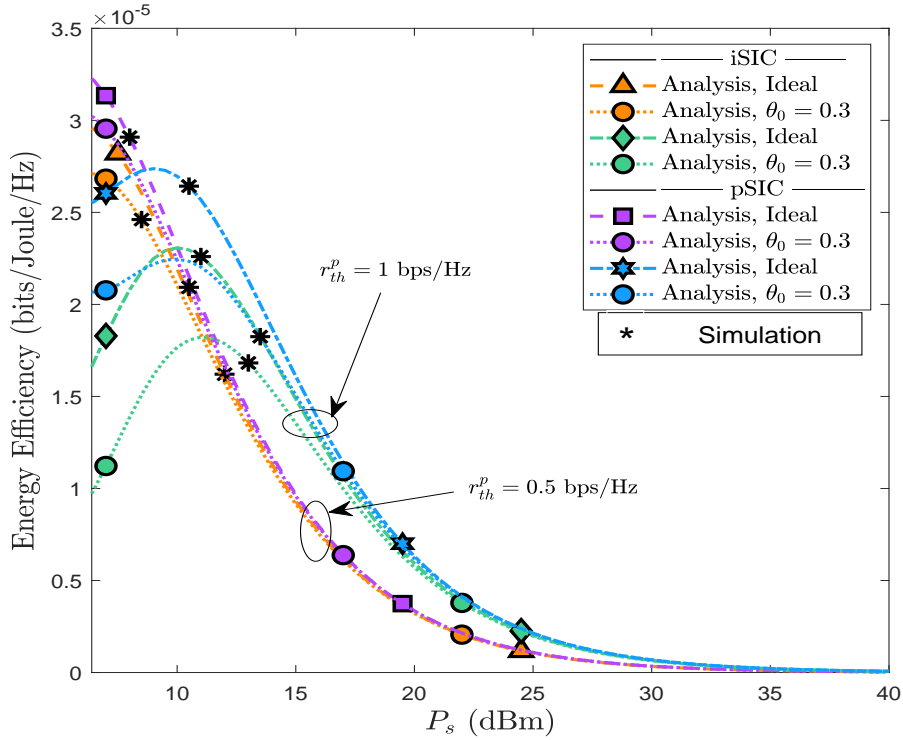


Figure 4.5: Energy efficiency plots for OC-NOMA system.

the I-CSST scheme with NOMA outperforms OMA for the high data rate needs. The theoretical findings presented in this research contribute to the development of design recommendations for upcoming wireless communication that will improve both energy efficiency and SE. Based on the results obtained, it was observed that the predictions generated by the DNN model for OP were highly consistent with the results obtained from the Monte-Carlo simulation and analysis. This suggests that utilizing a DNN model as a black box could be a potential and effective method for evaluating system performance in real network scenarios, without the need for complex and challenging equations with low-latency estimation.



This chapter presents the findings of the research conducted and suggests possible areas for future exploration.

## 5.1 Conclusions

A comprehensive performance analysis of an OC-NOMA system was presented in this thesis, which utilized EH-based SSC-DF schemes and considered the impact of practically induced iSIC and HIs on the transceiver nodes. By considering Nakagami- $m$  fading for terrestrial communication and Rician fading for air-to-ground communication channels, we assessed system throughput, OP for the primary and secondary networks, and energy efficiency to quantify the overall performance of the OCNOMA system. We also offered guidance for determining the appropriate NOMA power allocation factor to achieve effective SSC. The SSC-DF scheme has been demonstrated to outperform the benchmark PDT scheme, indicating that, it has relatively better performance. Compared to the PDT scheme, the SSC-DF scheme significantly enhances the outage performance of the secondary network. We assessed the effectiveness of the OC-NOMA system by examining the HD I-CSST scheme and factoring in the impact of HIs and iSIC. Our analysis included developing OP equations in closed-form for the primary and secondary networks in both Nakagami- $m$  fading and Rician fading scenarios, and the results were contrasted with the benchmark PDT and OMA I-CSST schemes. To gain additional perspectives, we also calculated the system's throughput and energy efficiency. We demonstrated that I-CSST performs better than benchmark PDT throughout the whole SNR range and is more resistant to HIs. Numerical results showed that the results of the Monte-Carlo simulation and analysis closely matched the outputs of

the DNN prediction for OP. Using a DNN as a black box could be a novel, efficient, and dependable approach to assess system efficacy. Employing a low-latency estimate method that does not call for the creation of difficult, complex equations in real-world network circumstances.

In order to provide insightful information about the practical design, we have thoroughly examined the OC-OMA system's performance. We have put up a number of plans and ideas that can boost the OC-NOMA system's SE and dependability and eventually make it easier to implement them in next-generation wireless systems.

## 5.2 Future Scope

- This thesis highlights several themes that are linked to the unresolved challenges of developing 6G communication technology. Future studies could address these issues, and the subsequent section offers some possible research directions.
- Future networks aim to achieve high spectrum efficiency, which is a crucial goal. The utilization of multiple input multiple output (MIMO) technology is employed to improve the spectrum efficiency and throughput of the OC-NOMA system. In MIMO systems, multiple antennas are utilized at the transceiver nodes to enable high data rate transmission.
- The presence of both PUs and SUs within the OC-NOMA system makes it susceptible to security threats. Hence, there is a critical need to devise physical layer security strategies for the OC-NOMA system. Addressing security breaches is a top priority in the development of 6G networks, which presents one of the significant challenges.
- Furthermore, we can also use TS protocol and can compare PS protocol with TS.
- Recent advancements in deep learning architectures and open-source AI/ML tools have led to increased attention towards utilizing AI/ML in wireless networks, particularly in NOMA. As a result, future research could focus on developing novel resource management algorithms assisted by ML, which can

effectively tackle the challenges posed by multi-dimensional and vast search spaces, as well as changing objectives and constraints.

- The current knowledge on the design of OC-NOMA system can be broadened by exploring the possibilities mentioned above.



## APPENDIX A

### DERIVATION OF (2.28)

The CDF  $F_{\gamma_{ru_1}^{\text{DF}}}(w) = \Pr[\gamma_{ru_1}^{\text{DF}} < w]$  is expressed, using (2.17), as

$$\begin{aligned} F_{\gamma_{ru_1}^{\text{DF}}}(w) &= \Pr \left[ \frac{\delta \beta \Delta_s |g_{sr}|^2 |g_{ru_1}|^2}{\beta \Delta_s |g_{sr}|^2 |g_{ru_1}|^2 \Xi_p + 1} < w \right] \\ &= \Pr \left[ |g_{sr}|^2 < \frac{w}{\beta \Delta_s (\delta - \Xi_p w) |g_{ru_1}|^2} \right], \end{aligned} \quad (\text{A.1})$$

which can be further simplified as

$$F_{\gamma_{ru_1}^{\text{DF}}}(w) = \int_0^\infty \left( \int_0^{T_1 y^{-1}} f_{|g_{sr}|^2}(x) dx \right) f_{|g_{ru_1}|^2}(y) dy. \quad (\text{A.2})$$

On substituting the expression of PDFs using (2.5) and solving using [39, eq. 1.111], one can reach at the desired result in (2.28).

## APPENDIX B

### DERIVATION OF (2.41)

Now taking  $P_2 = \Pr[\tau_p - \gamma_{ru_2, x_s}^{\text{DF}} \leq \gamma_{su_2}^{\text{DT}}, \tau_s \leq \gamma_{ru_2}^{\text{DF}}]$ , inserting the appropriate SNDR expressions from (2.8), (2.18), and (2.19) and retrieving the  $|h_{ru_2}|^2$  condition to get the expression in (2.41), we can perform an analysis for  $\tau_p < \gamma_{ru_2, x_s}^{\text{DF}}$  and  $\tau_p > \gamma_{ru_2, x_s}^{\text{DF}}$ . The term  $P_{21} = 1 - \Pr[\gamma_{su_2}^{\text{DT}} < \tau_p - \gamma_{ru_2, x_s}^{\text{DF}}]$  can be evaluated in this case utilising the  $L$ -stairways conjecture to get the result in (2.42). In contrast, the  $P_{22} = \Pr[\gamma_{ru_2}^{\text{DF}} \geq \tau_s] = 1 - F_{\gamma_{ru_2}^{\text{DF}}}(x)$  can be assessed for  $T_5 > 0$  as

$$P_{22} = 1 - \int_0^\infty \int_{\frac{T_6 z}{T_5}}^\infty \int_0^{\frac{\tau_s}{T_4(T_5 y - T_6 z)}} f_{|g_{sr}|^2}(x) f_{|g_{ru_2}|^2}(y) \times f_{|h_I|^2}(z) dx dy dz. \quad (\text{B.1})$$

On substituting the expression of PDF  $f_{|g_{sr}|^2}(x)$  and solving the inner integral using [39, eq. 3.351.1], (B.1) can be simplified as  $P_{22} = \int_0^\infty (\mathbb{B}_1(\tau_s) - \mathbb{B}_2(\tau_s)) f_{|h_I|^2}(z) dz$ , where

$$\mathbb{B}_1(\tau_s) = \int_{\frac{T_6 z}{T_5}}^\infty \sum_{l=0}^\infty \frac{K_{ru_2}^l}{(l!)} e^{-K_{ru_2}} f_{|g_{ru_2}|^2}(y) dy \quad (\text{B.2})$$

and

$$\mathbb{B}_2(\tau_s) = \int_{\frac{T_6 z}{T_5}}^\infty \sum_{l=0}^\infty \sum_{a=0}^l \frac{K_{ru_2}^l b_{ru_2}^a}{(l!)(a!)} \left(\frac{\tau_s}{T_4}\right)^a e^{-K_{ru_2}} f_{|g_{ru_2}|^2}(y) dy. \quad (\text{B.3})$$

Thus, on invoking the expression of PDFs  $f_{|g_{ru_2}|^2}(y)$  and  $f_{|h_I|^2}(z)$ , and solving the associated integral with the help of [39, eq. 3.351.2] and [39, eq. 3.351.3], we obtain  $P_{22}$  as presented in (2.43).



## REFERENCES

- [1] G. Gui, M. Liu, F. Tang, N. Kato, and F. Adachi, “6G: Opening new horizons for integration of comfort, security, and intelligence,” *IEEE Wireless Commun.*, vol. 27, no. 5, pp. 126-132, Oct. 2020.
- [2] M. B. Pandian, M. L. Sichitiu, and H. Dai, “Optimal resource allocation in random access cooperative cognitive radio networks,” *IEEE Trans. Mobile Comp.*, vol. 14, no. 6, pp. 1245-1258, Jun. 2015.
- [3] F. Shan, J. Luo, W. Wu, M. Li, and X. Shen, “Discrete rate scheduling for packets with individual deadlines in energy harvesting systems,” *IEEE J. Sel. Areas Commun.*, vol. 33, no. 3, pp. 438-451, Mar. 2015.
- [4] D. Gao, L. Wang, and B. Hu, “Spectrum efficient communication for heterogeneous IoT networks,” *IEEE Trans. Netw. Sci. Eng.*, vol. 9, no. 6, pp. 3945-3955, Nov.-Dec. 2022.
- [5] T. Wu and H. -C. Yang, “RF energy harvesting with cooperative beam selection for wireless sensors,” in *Proc. IEEE Wireless Commun. Lett.*, vol. 3, no. 6, pp. 585-588, Dec. 2014,
- [6] H. -V. Tran and G. Kaddoum, “Robust design of AC computing-enabled receiver architecture for SWIPT networks,” *IEEE Wireless Commun. Lett.*, vol. 8, no. 3, pp. 801-804, Jun. 2019.

- [7] M. Bouabdellah *et al.*, “Cooperative energy harvesting cognitive radio networks with spectrum sharing and security constraints,” *IEEE Access*, vol. 7, pp. 173329-173343, Nov. 2019.
- [8] R. C. Qiu *et al.*, “Cognitive radio network for the smart grid: Experimental system architecture, control algorithms, security, and microgrid testbed,” *IEEE Trans. Smart Grid.*, vol. 2, no. 4, pp. 724-740, Dec. 2011.
- [9] S. Thakur and A. Singh, “Secrecy performance of underlay cognitive radio networks with primary interference,” *IEEE Trans. Netw. Sci. Eng.*, vol. 9, no. 4, pp. 2641-2657, 1 Jul.-Aug. 2022.
- [10] D. K. Verma, R. Y. Chang, and F. -T. Chien “Energy-assisted decode-and-forward for energy harvesting cooperative cognitive networks,” *IEEE Trans. Cogn. Commun. and Netw.*, vol. 3, no. 3, pp. 328-342, Sep. 2017.
- [11] J. He, S. Guo, G. Pan, Y. Yang, and D. Liu, “Relay cooperation and outage analysis in cognitive radio networks with energy harvesting,” *IEEE Syst. Journ.*, vol. 12, no. 3, pp. 2129-2140, Sep. 2018.
- [12] Z. Ding *et al.*, “A survey on non-orthogonal multiple access for 5G networks: Research challenges and future trends,” *IEEE J. Sel. Areas Commun.*, vol. 35, no. 10, pp. 2181-2195, Oct. 2017.
- [13] Y. Liu, Z. Ding, M. ElKashlan, and J. Yuan, “Non-orthogonal multiple access in large-scale underlay cognitive radio networks,” *IEEE Trans. Veh. Technol.*, vol. 65, no. 12, pp. 10152-10157, Dec. 2016.
- [14] L. Lv, J. Chen, Q. Ni, Z. Ding, and H. Jiang, “Cognitive non-orthogonal multiple access with cooperative relaying: A new wireless frontier for 5G spectrum sharing,” *IEEE Commun. Mag.*, vol. 56, no. 4, pp. 188-195, Apr. 2018.
- [15] S. Arzykulov, G. Nauryzbayev, T. A. Tsiftsis, B. Maham, and M. Abdallah, “On the outage of underlay CR-NOMA networks with detect-and-forward relaying,” *IEEE Trans. Cogn. Commun. Netw.*, vol. 5, no. 3, pp. 795-804, Sep. 2019.

- [16] L. Lv, Q. Ni, Z. Ding, and J. Chen, "Application of non-orthogonal multiple access in cooperative spectrum-sharing networks over Nakagami- $m$  fading channels," *IEEE Trans. Veh. Technol.*, vol. 66, no. 6, pp. 5510-5515, Jun. 2017.
- [17] X. Zhang *et al.*, "Outage performance of NOMA-based cognitive hybrid satellite-terrestrial overlay networks by amplify-and-forward protocols," *IEEE Access*, vol. 7, pp. 85372-85381, Jun. 2019.
- [18] V. Singh, P. K. Upadhyay, and M. Lin, "On the performance of NOMA-assisted overlay multiuser cognitive satellite-terrestrial networks," *IEEE Wireless Commun. Lett.*, vol. 9, no. 5, pp. 638-642, May 2020.
- [19] Y. Xu *et al.*, "Joint beamforming and power-splitting control in downlink cooperative SWIPT NOMA systems," *IEEE Trans. Signal Process.*, vol. 65, no. 18, pp. 4874-4886, Sep. 2017.
- [20] D. Wang and S. Men, "Secure energy efficiency for NOMA based cognitive radio networks with nonlinear energy harvesting," *IEEE Access*, vol. 6, pp. 62707-62716, Oct. 2018.
- [21] A. K. Shukla, J. Sharanya, K. Yadav, and P. K. Upadhyay, "Exploiting SWIPT-enabled IoT-based cognitive nonorthogonal multiple access with coordinated direct and relay transmission," *IEEE Sensor J.*, vol. 22, no. 19, pp. 18988-18999, Oct. 2022.
- [22] Y. Yu, Z. Yang, Y. Wu, J. A. Hussein, W. -K. Jia, and Z. Dong, "Outage performance of NOMA in cooperative cognitive radio networks with SWIPT," *IEEE Access*, vol. 7, pp. 117308-117317, Sep. 2019.
- [23] C. K. Singh and P. K. Upadhyay, "Overlay cognitive IoT-based full-duplex relaying NOMA systems with hardware imperfections," *IEEE Internet Things J.*, vol. 9, no. 9, pp. 6578-6596, May 2022.
- [24] H. Huang *et al.*, "Deep learning for physical-layer 5G wireless techniques:

- Opportunities, challenges and solutions,” *IEEE Wireless Commun.*, vol. 27, no. 1, pp. 214-222, Feb. 2020.
- [25] T. -H. Vu, T. -V. Nguyen, and S. Kim, “Wireless powered cognitive NOMA-based IoT relay networks: Performance analysis and deep learning evaluation,” *IEEE Internet Things J.*, vol. 9, no. 5, pp. 3913-3929, Mar. 2022.
- [26] Z. Zhang, Y. Lu, Y. Huang, and P. Zhang, “Neural network-based relay selection in two-way SWIPT-enabled cognitive radio networks,” *IEEE Trans. Veh. Technol.*, vol. 69, no. 6, pp. 6264-6274, Jun. 2020.
- [27] G. Gui, H. Huang, Y. Song, and H. Sari, “Deep learning for an effective non-orthogonal multiple access scheme,” *IEEE Trans. Veh. Technol.*, vol. 67, no. 9, pp. 8440-8450, Sep. 2018.
- [28] G. Manogaran, T. N. Nguyen, J. Gao, and P. M. Kumar, “Deep learning-based service distribution model for wireless network assisted internet of everything,” *IEEE Trans. Netw. Sci. Eng.*, vol. 9, no. 5, pp. 3004-3014, Sep.-Oct. 2022.
- [29] X. Li, J. Li, Y. Liu, Z. Ding, and A. Nallanathan, “Residual transceiver hardware impairments on cooperative NOMA networks,” *IEEE Trans. Wireless Commun.*, vol. 19, no. 1, pp. 680-695, Jan. 2020.
- [30] C. K. Singh, V. Singh, P. K. Upadhyay, and M. Lin, “Energy harvesting in overlay cognitive NOMA systems with hardware impairments,” *IEEE Syst. Journ.*, vol. 16, no. 2, pp. 2648-2659, Jun. 2022.
- [31] E. Bjornson, P. Zetterberg, M. Bengtsson, and B. Ottersten, “Capacity limits and multiplexing gains of MIMO channels with transceiver impairments,” *IEEE Commun. Lett.*, vol. 17, no. 1, pp. 91-94, Jan. 2013.
- [32] V. Singh, S. Solanki, P. K. Upadhyay, D. B. da Costa, and J. M. Moualeu, “Performance analysis of hardware-impaired overlay cognitive satellite-terrestrial networks with adaptive relaying protocol,” *IEEE Syst. Journ.*, vol. 1, no. 15, pp. 192-203, Mar. 2021.

- [33] G. Im and J. H. Lee, "Outage probability for cooperative NOMA systems with imperfect SIC in cognitive radio networks," *IEEE Commun. Lett.*, vol. 23, no. 4, pp. 692-695, Apr. 2019.
- [34] D. -T. Do, A. -T. Le, and B. M. Lee, "NOMA in cooperative underlay cognitive radio networks under imperfect SIC," *IEEE Access*, vol. 68, no. 8, pp. 4709-4722, Aug. 2020.
- [35] S. Arzykulov *et al.*, "Hardware- and interference-limited cognitive IoT relaying NOMA networks with imperfect SIC over generalized non-homogeneous fading channels," *IEEE Access*, vol. 8, pp. 72942-72956, Apr. 2020.
- [36] S. Ghosh, A. Al-Dweik, and M. -S. Alouini, "On the performance of end-to-end cooperative NOMA-based IoT networks with wireless energy harvesting," *IEEE Internet Things J.*, doi: 10.1109/JIOT.2023.3267564, Apr. 2023.
- [37] S. Jeong, O. Simeone, and J. Kang, "Mobile edge computing via a UAV mounted cloudlet: Optimization of bit allocation and path planning," *IEEE Trans. Veh. Technol.*, vol. 67, no. 3, pp. 2049-2063, Mar. 2018.
- [38] M. Dai, Y. Wu, L. Qian, Z. Su, B. Lin, and N. Chen, "UAV-assisted multi-access computation offloading via hybrid NOMA and FDMA in marine networks," *IEEE Trans. Netw. Sci. Eng.*, vol. 10, no. 1, pp. 113-127, Jan.-Feb. 2023.
- [39] I. S. Gradshteyn and I. M. Ryzhik, *Tables of Integrals, Series and Products*, 6th ed. New York: Academic Press, 2000.
- [40] S. Solanki, J. Park, and I. Lee, "On the performance of IRS-aided UAV networks with NOMA," *IEEE Trans. Veh. Technol.*, vol. 71, no. 8, pp. 9038-9043, Aug. 2022.
- [41] C. Zhang, J. Ge, J. Li, Y. Rui, and M. Guizani, "A unified approach for calculating outage performance of two-way AF relaying over fading channels," *IEEE Trans. Veh. Technol.*, vol. 64, no. 3, pp. 1218-1229, Mar. 2015.

- [42] X. Yue, Y. Liu, S. Kang, A. Nallanathan, and Z. Ding, "Exploiting full/half-duplex user relaying in NOMA systems," *IEEE Trans. Commun.*, vol. 66, no. 2, pp. 560-575, Feb. 2018.
- [43] *8 Hints for making and interpreting EVM measurements*, Tech. Rep., Agilent Technologies, Santa Clara, CA, USA, 2005.



# List of Publications

## Publications from MS(Research) Thesis Work

### In Refereed Journals

1. **R. Kumar**, C. K. Singh, P. K. Upadhyay, A. M. Salhab, A. A. Nasir, and M. M. Ali, "IoT-Inspired Cooperative Spectrum Sharing with Energy Harvesting in UAV-Assisted NOMA Networks: Deep Learning Assessment," ***IEEE Internet of Things Journal***, (Under review), **Impact Factor: 10.238**.